Rare-Earth Nickelates $RNiO_3$: Thin films and heterostructures

Catalano, Sara; Gibert Gutierrez, Marta; Fowlie, Jennifer; Iniguez, Jorge; Triscone, Jean-Marc; Kreisel, Jens

How to cite

CATALANO, Sara et al. Rare-Earth Nickelates $RNiO_3$: Thin films and heterostructures. In: Reports on Progress in Physics, 2018, vol. 81, n° 046501.

This publication URL: https://archive-ouverte.unige.ch/unige:103464

Rare-Earth Nickelates $RNiO_3$: Thin films and heterostructures

S. Catalano[1], M. Gibert[1], J. Fowlie[1], J. Íñiguez[2], J.-M. Triscone[1], J. Kreisel[2,3,*]

[1] DQMP, Université de Genève, 24 Quai Ernest-Ansermet, 1211 Geneva, Switzerland

[2] Materials Research and Technology Department, Luxembourg Institute of Science and Technology, 41 Rue du Brill, 4422 Belvaux, Luxembourg

[3] Physics and Materials Science Research Unit, University of Luxembourg, 41 Rue du Brill, 4422 Belvaux, Luxembourg

* jens.kreisel@list.lu

Abstract

This review stands in the larger framework of functional materials by focussing on heterostructures of Rare-Earth Nickelates, described by the chemical formula $RNiO_3$ where R is a trivalent rare-earth $R = La, Pr, Nd, Sm, ..., Lu$. Nickelates are characterized by a rich phase diagram of structural and physical properties and serve as a benchmark for the physics of phase transitions in correlated oxides where electron-lattice coupling plays a key role. Much of the recent interest in nickelates concerns heterostructures, that is single layers of thin film, multilayers or superlattices, with the general objective of modulating their physical properties through strain control, confinement or interface effects. We will discuss the extensive studies on nickelate heterostructures as well as outline different approaches to tuning and controlling their physical properties and, finally, review application concepts for future devices.

Outline

1. Introduction

2. ABO_3 perovskites
   - 2.1 Structure, symmetry and oxygen octahedra rotations
   - 2.2 d-orbital physics
   - 2.3 Metal-to-Insulator Transition: Mott insulator and charge transfer insulator

3. *R*NiO_3 Nickelates

- 3.1 Phase diagram
- 3.2 Basic electronic configuration
- 3.3 Metal-to-Insulator Transition (MIT)
- 3.4 Magnetic Néel transition
- 3.5 Behavior under pressure
- 3.6 Behavior under magnetic fields, multiferroic effects
- 3.7 Theory

4. *R*NiO_3 thin films

- 4.0 Motivation
- 4.1 Control of the Metal-to-Insulator Transition
  - 4.1.1 Strain engineering
  - 4.1.2 Influence of the substrate orientation
  - 4.1.3 Chemical doping effects
  - 4.1.4 Electric field effect
  - 4.1.5 Pump-probe experiments
- 4.2 The case of $LaNiO_3$

5. Thin film multilayers

- 5.0 Motivation
- 5.1 $LaNiO_3$-based multilayers
- 5.2 *R*NiO_3-based multilayers

6. Scope of applications

- 6.0 Context
- 6.1 Exploiting the conductivity of $LaNiO_3$
- 6.2 Exploiting the metal-to-insulator transition and associated properties
  - 6.2.1 Resistance Switching
  - 6.2.2 Opto-electronic properties
- 6.3 Magnetic properties

7. Wrap-up and outlook

1. INTRODUCTION

This review stands in the larger framework of research on functional materials. A material can be considered functional if it possesses a property that can be tuned, making it particularly appealing for application.

Among functional materials, correlated transition metal oxides (TMOs) have attracted particular attention due to their remarkable structural, electronic, magnetic and optical properties. Such a range of behavior expands the potential for the development of novel electronic architectures. A distinctive feature of complex TMOs is the competition between electronic phases close to phase boundaries, which are often highly sensitive to subtle structural changes and, in this way, a method of fine control is provided. In conjunction with the increasing interest in the understanding and implementation of TMOs, recent years have seen great advances in the growth of high quality epitaxial TMO heterostructures. This includes the fabrication of digital oxide heterostructures, making possible the manipulation of the the electronic states of TMOs by exploiting interface-induced phenomena and reduced dimensionality. Such epitaxial heterostructures have allowed for the discovery of new, and elucidation of existing, physical phenomena to the point where it is now realistic to envisage oxide electronic devices with the potential to compete with semiconductor architectures [1-4].

In this review, we focus on the family of perovskite nickelates, which is described by the chemical formula $R\mathrm{NiO_3}$, where R is a trivalent rare-earth $R = La, Pr, Nd, Sm, ..., Lu$. These nickelates are characterized by a rich landscape of structural and physical properties. The phase diagram of the $R\mathrm{NiO_3}$ family stands as a canonical example of the physics of phase transitions in correlated oxides to which the electron-lattice coupling contributes significantly. One of the main characteristics of nickelates, with the exception of $R = La$, is a sharp metal-to-insulator transition (MIT), which is mainly determined by the Ni-O-Ni bond angle. As a result, the physical properties of perovskite nickelates can be modulated by a large variety of parameters ranging from temperature, pressure and R-size, to epitaxial strain in heterostructures, and also stoichiometry or electrostatic doping.

Much of the recent interest in nickelates is focused on thin films and their integration into superlattices with the general objective of modulating their physical properties through strain control, confinement and interface effects. Moreover, due to the lack of sizeable nickelate single crystals, epitaxial thin films also constitute the best system in which to study the fascinating physics of these compounds.

The nickelate family has previously been reviewed by Medarde[5], Catalan[6] and, more recently, Middey *et al.*[7]. Here we focus on perovskite nickelates and their properties in heterostructure form – both single layers and multilayers, or superlattices. We also detail various strategies that allow their properties to be tuned and controlled and the applicability of these materials in future devices.

2. ABO_3 PEROVSKITES

2.1 Structure, symmetry and oxygen octahedral rotations

Perovskite oxides are characterized by the chemical formula ABO_3, where A and B are two cations, with A larger than B, and O is an oxygen anion. The ideal perovskite structure is cubic with space group Pm-3m, as illustrated in Fig. 1a. The B cations (represented in orange) are 6-fold coordinated with the O anions (red), forming the BO_6 octahedra that constitute the fundamental structural and functional unit of perovskites. The octahedral units form a three-dimensional corner-sharing network, with the A cations (purple) arranged in the cavities and 12-fold coordinated with the oxygens. The resulting crystal lattice structure is highly stable and the A and B sites can each support a wide variety of elements, enriching this family of materials with a *plethora* of properties [8].

Ideally, for the cubic unit cell shown in Fig. 1a, the lattice parameter a and the ionic radii r_i should satisfy the relation $a = \sqrt{2}(r_A + r_O) = 2(r_B + r_O)$, where r_A, r_B and r_O denote the radii of the A, B and O ions, respectively. In reality, for most of the perovskite compounds this relation does not hold and structural distortions occur in order to optimize the ionic packing, bringing the system away from the cubic ideal. The tendency to distort can be estimated by the Goldschmidt tolerance factor t, defined as:

$$t = \frac{(r_A + r_O)}{\sqrt{2}(r_B + r_O)}$$

For $0.9 < t < 1$, the cubic perovskite structure is stable in most cases, although, some compounds relax to a rhombohedral symmetry. For $t < 0.9$, the crystal tends to adopt either a rhombohedral or an orthorhombic structure (see Fig. 1b). For $t > 1$, perovskites usually develop a ferroelectric instability and, when t is increased even further, they crystallize as a hexagonal polymorph. The most typical structural distortions of the cubic lattice can be described by displacements of the A cations in combination with rotations, or tilts, and distortions of the corner-sharing BO_6 units. Fig. 1e illustrates the octahedral tilts leading to an orthorhombic structure from the cubic one (Figure 1d). The symmetry-allowed rigid rotations of BO_6 octahedra in ABO_3 compounds have been classified by the pioneering studies of Glazer [9,10], where he showed that the most common

distortions of the BO_6 network can be described as simple octahedral rotations α, β, γ about the x, y, z principal crystallographic axes of the perovskite lattice, respectively, as in Fig. 1c.

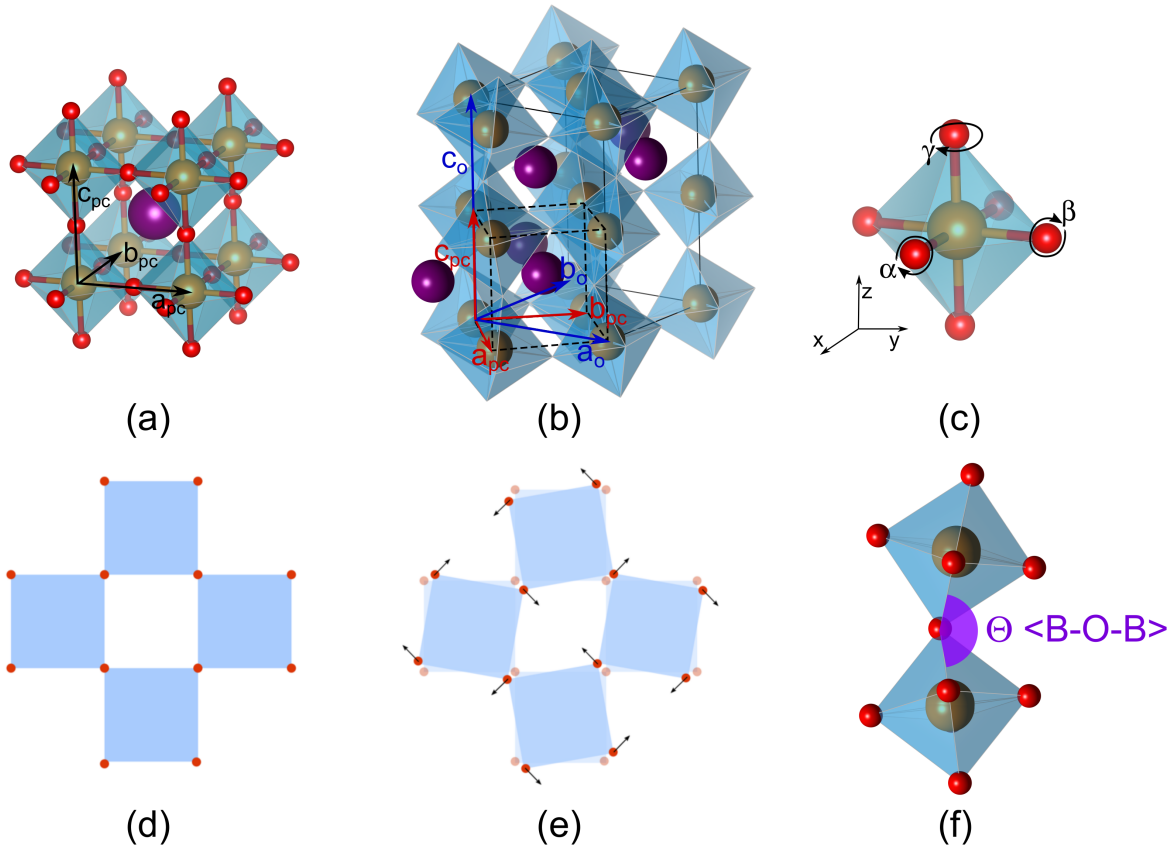

Figure 1: Perovskite ABO_3 structure. (a) cubic and (b) orthorhombic unit cells. In (b) the relationship between the pseudocubic and the orthorhombic unit cells is sketched. (c) Illustration of the tilt axes identified in Glazer notation [10]. Top views of the corner-sharing BO_6 units in the (d) cubic and (e) orthorhombic structure. (f) Schematic of the oxygen octahedral network with the apical <B-O_{apical}-B> angle Θ indicated. In all panels, the A cation is the orange central sphere, the B cations are the purple spheres arranged at the corner of the cubic unit cell and 6-fold coordinated with the O anions (red).

Often, the degree of distortion of perovskite compounds is also quantified by means of the weighted average B-O-B bond angle Θ, illustrated in Fig. 1f, which scales proportionally with t [11]. Notice that there are two distinct B-O-B angles within the *Pbnm* structure, corresponding to the two distinct oxygen positions: 2 out-of-plane B-O_{apical}-B and 4 in-plane B-O_{basal}-B angles.

Regardless of the specific structure adopted, it is convenient to describe the actual material with respect to the five atom *pseudocubic* (pc) unit cell that is common to all the perovskite compounds. For example, it is useful to compare the pc-lattice parameter, a_{pc}, of different compounds, in order to assess their structural similarity. The relationship between the *pseudocubic* and *orthorhombic* unit cells is sketched in Fig.1b.

2.2 d orbital physics

As previously mentioned, a characteristic property of ABO_3 compounds is that they are structurally stable for a wide variety of cations on the A and B sites. In particular, perovskites with a transition metal on the B site display a remarkable range of electronic phases arising from the rich physics of the *d* electrons and the fact that their overlap, either direct or through the oxygen 2*p* orbitals, can be tuned by structural changes.

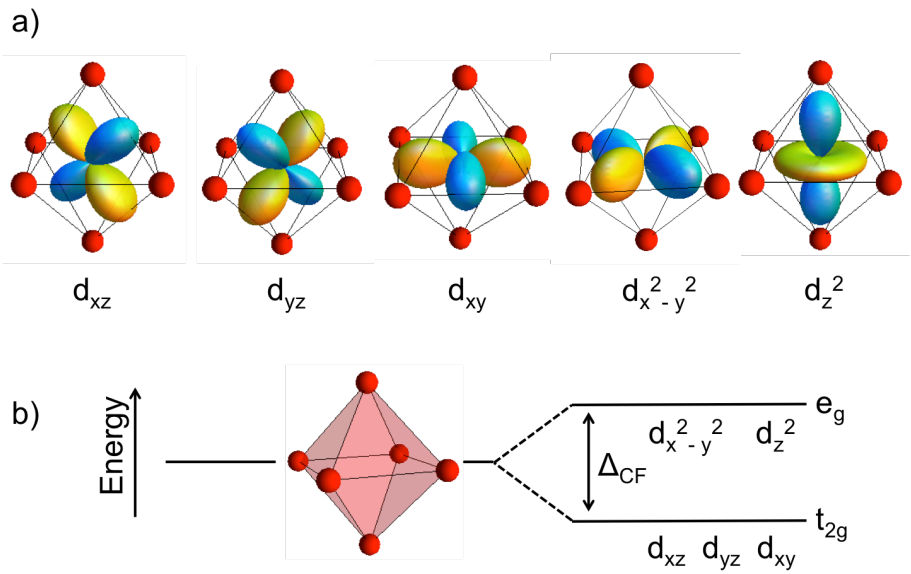

Figure 2: 3*d* orbitals. (a) Illustration of the 3d wave functions, with respect to the ligand oxygen positions. The colors correspond to the different sign, or phase, of the wave functions. (b) Octahedral crystal field splitting Δ_{CF} of the 3*d* orbitals.

3*d* orbitals form in five distinct wave functions, illustrated in Fig. 2a. In the ABO_3 compounds, the six oxygen anions surrounding the B cation produce an octahedral crystal field, which lifts the degeneracy of the *d* orbitals. As a result, the wave functions that point toward the oxygen sites (e_g) are lifted in energy above those directed towards the space between oxygen sites (t_{2g}), as shown in Fig. 2b. Furthermore, as *d* states are spatially confined, TMOs are characterized by strong electronic correlations, U, with respect to the material bandwidth, W. Such a large *U*:*W ratio* can eventually bring about a Mott transition in open-shell systems, as discussed later.

Inter-site hopping and magnetic interactions are established through the overlap between the B site *d* wave functions and the *p* wave functions of the O^{2-} anions. The properties of ABO_3 compounds are, therefore, easily manipulated by tilting and deforming of the BO_6 units. In fact, as

both oxygen *p* and transition metal *d* orbitals are highly directional, even subtle changes in the ABO_3 structure will influence the charge, orbital and spin degrees of freedom of the system, and vice versa. This high level of interplay between so many parameters is at the origin of the variety of electronic phases observed in perovskite compounds[12]. In the following section, we will focus on a particular example of electronic phase transition: the metal-to-insulator transition.

2.3 Metal-to-Insulator Transition: Mott Insulator and Charge Transfer Insulator

Some perovskite oxides display characteristic metal-to-insulator transitions (MITs) driven by strong electronic interactions associated to the *d* wave functions, such as the Coulomb repulsion and Hund's coupling. Such compounds are often insulating despite the fact that the number of electrons (*n*) in the system corresponds to a partially filled *d* shell of the B cation [13]. The transition from an itinerant to a localized electronic regime was originally addressed by Mott and Hubbard in the famous *Hubbard model* [14,15]. The Hubbard model describes electrons moving in a periodic lattice, with a single level at each site, and forming a single electronic band. As electrons hop from site *i* to site *j*, the system is left with one unoccupied *i* site and a doubly occupied *j* site. Mott pointed out that the double occupancy costs a finite energy due to the charge repulsion between the electrons, namely, the Coulomb interaction *U*. Then, if *U* is comparable to the kinetic energy of the system, an MIT can occur as a function of *U* at half-filling. Introducing the Coulomb interaction, the system can be described by the *Hubbard Hamiltonian*:

$$\mathcal{H} = -t \sum_{(i,j),\sigma} c_{i,\sigma}^{\dagger} c_{j,\sigma} + U \sum_i n_{i,\uparrow} n_{i,\downarrow} ,$$

where the first term represents the inter-site hopping of electrons and the second one takes into account the onsite electron repulsion. As the onsite interaction strength is increased, the original single band splits into two distinct bands, the lower Hubbard (LH) and upper Hubbard (UH) band, and a charge gap opens, as shown in Fig. 3a.

The Hubbard model describes the behavior of a system of particles (electrons) moving in a periodic potential and occupying a single Bloch band. Yet, the model can be extended in order to describe more complex systems, in which electronic interactions and multi-orbital occupation contribute to the physics as well. The extended Hubbard model correctly describes the properties of several oxide compounds (e.g. titanates, vanadates), characterized by a rich *spectrum* of *d-d* inter- and intra-orbital excitations, which are classified as *Mott-Hubbard insulators*. On the other hand, many oxides based on heavy transition metal elements, such as Ni or Cu, display an insulating behavior that cannot be described in terms of *d-d* excitations alone. For these compounds, the *d*

band of the transition metal ions lies close to the *p* band of the ligand oxygen ions, which mediate the inter-site hopping of the electrons. Within this context, the lowest energy charge excitation is the transfer of an electron from the *p* band to the *d* orbitals, leaving one ligand hole *L* in the oxygen band and *n+1* electrons at the transition metal site:

$$d^n \rightarrow d^{n+1}L.$$

The energy required for this kind of excitation constitutes the *charge transfer* (CT) gap, Δ, which can be viewed as the energy separation between the centers of mass of the oxygen *p* band and the transition metal upper Hubbard band, see Fig. 3b. Materials complying with this picture are known as *charge-transfer insulators*.

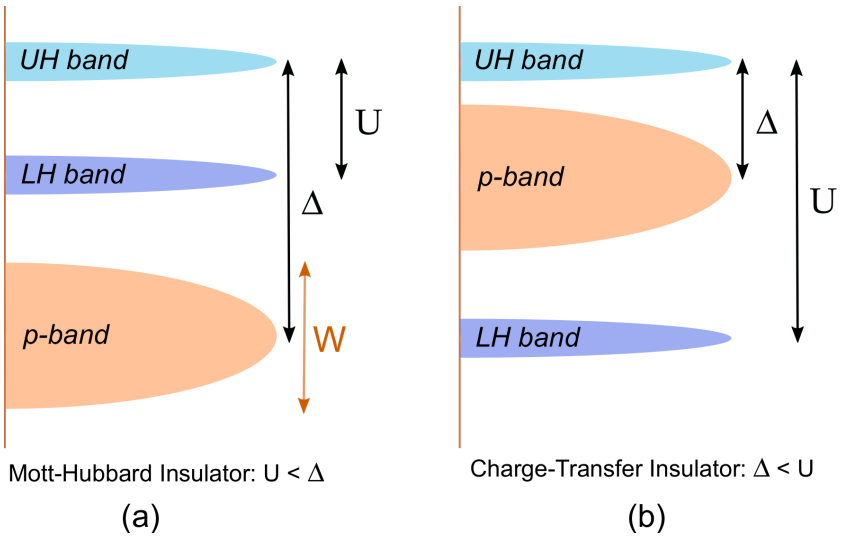

Figure 3: Schematic band structure of (a) a Mott-Hubbard insulator and (b) a charge-transfer insulator.

The difference between the Mott-Hubbard-type and CT-type of insulators is sketched in Fig. 3. In the former, the MIT is controlled by the Coulomb interaction, *U*, which is the energy required for the process $d_i^n + d_j^n \rightarrow d_i^{n+1} + d_j^{n-1}$, while in the latter the MIT is controlled by the CT energy, Δ, corresponding to the process $d^n \rightarrow d^{n+1}L$. These energy scales are to be compared to the system bandwidth, *W*. As *W* decreases, the gap opens and the material tends to become an insulator. For a Mott-Hubbard insulator, $U < \Delta$ and the gap energy E_{gap} is directly proportional to *U*; in contrast, for a CT-insulator $\Delta < U$ and $E_{gap} \propto \Delta$.

This model, introduced by Zaanen, Sawatzky and Allen and called the ZSA scheme [16], correctly predicts the ground state of many TMOs. In this work, the authors propose that either a Mott-like or a CT-like insulating gap is opened, depending on the ratio between the Coulomb interaction *U* and the CT energy Δ. For small values of both *U* and Δ, metallic behavior is expected

Finally, some TMOs are found to be insulating even though they are predicted to be metallic according to the ZSA scheme. In fact, the CT energy decreases systematically as the valence of the TM ion increases [17]. TM compounds with unusually high valence, such as Cu^{3+}, Ni^{3+} and Fe^{4+}, are expected to be characterized by low, or even negative, Δ and, therefore, should display metallic behavior. Instead, some of these compounds, such as $NaCuO_2$, $LiNiO_2$,$CaFeO_3$ and all the rare earth nickelates except $LaNiO_3$, are insulators at low temperature [18]. The nature of these insulators was first unveiled by Mizokawa *et al.* who, through a detailed analysis of the x-ray photoemission and absorption spectra of $NaCuO_2$ [18,19], concluded that the CT energy should be close to zero and comparable to the *p-d* hybridization strength. It was shown that, for this compound, the ground state is characterized by a dominant contribution of the $d^{n+1}L$ electronic configuration, strongly hybridized with the d^n state. While the $d^{n+1}L$ configuration is typically described as a continuum of states, the strong *p-d* hybridization causes a localized state with $d^{n+1}L$ character to be split off from the continuum. Then, the insulating gap is found to be proportional to the hybridization strength and the lowest energy charge excitation corresponds to the process:

$$(d^{n+1}L)_i + (d^{n+1}L)_j \rightarrow (d^{n+1}L^2)_i + (d^{n+1})_j ,$$

meaning that the gap has a *p-p* character. As a consequence, Mizokawa *et al.* proposed an extension of the ZSA diagram including the *negative CT insulators*, identified by a small or negative Δ value, as compared to the *p-d* hybridization strength and the Coulomb interaction *U*. As discussed later, the perovskite nickelates belong to this region of the phase diagram and display an insulating ground state, making them a notable example of a negative CT system.

3. *R*NiO_3 NICKELATES

3.1 Phase diagram

The perovskite nickelate family is characterized by the chemical formula *R*NiO_3 where *R* is a trivalent rare earth *R = La, Pr, Nd, Sm, ..., Lu*. The physical and structural properties of these compounds are summarized in the phase diagram displayed in Fig. 4, parameterized by temperature and *R* size. One of the main characteristics of *R*NiO_3s, with the exception of *R = La*, is a sharp metal-to-insulator transition (MIT) as the temperature is reduced, with the transition temperature decreasing as the size of the *R* cation increases [5,6,20]. Equivalently, the evolution of the MIT can be correlated to the Goldschmidt tolerance factor t, as described in section 2.1. The decrease of the tolerance factor with *R* size tends to reduce the Ni-O-Ni angle, Θ, with a consequent reduction of the overlap between the Ni-3*d* and O-*p* orbitals. Therefore, the Ni-O-Ni bond angle is also often taken as the control parameter in the nickelate phase diagram.

For a long time, the crystal structure of the RNiO$_3$ family was thought to be orthorhombic (space group *Pbnm*) in both the metallic and the insulating regimes, except for the case of LaNiO$_3$, which crystalizes in a rhombohedral structure (*R-3c* space group). It was recognized early on that the MIT is concomitant with an expansion of the unit cell volume of about 0.2 %, and that sharp MITs are often accompanied by a structural phase transition. This phase transition was observed by neutron diffraction and high-resolution x-ray diffraction experiments, which revealed two distinguishable NiO$_6$ octahedral groups in the insulating phase, leading to a monoclinic distortion and a space group $P2_1/n$ [21-24]. This structural transition can be seen as a cooperative breathing distortion of the oxygen octahedra, which alternately contract and expand in a three-dimensional checkerboard pattern. Consequently, the insulating phase is characterized by a Ni-O bond length disproportionation (BD) with two inequivalent Ni sites, as illustrated in Fig. 5. These distinct Ni-O bonds are crucial for the occurrence of the MIT according to the most recent theoretical models (see section 3.7) [25-32].

At high temperature, RNiO$_3$ compounds are metallic and paramagnetic, whereas the insulating ground state is antiferromagnetic. For *R = Nd, Pr*, the MIT occurs simultaneously with a Néel transition from the paramagnetic to the antiferromagnetic state; in contrast, for $r_A \leq r_{Sm}$ the MIT and spin-ordering transitions take place at different temperatures, with $T_{Néel} < T_{MI}$. Furthermore, measurements of resistivity versus temperature of both NdNiO$_3$ and PrNiO$_3$ exhibit a clear hysteresis of the MIT, indicative of a first-order transition, while barely any hysteretic behavior is observed for the members of the family with $r_A \leq r_{Sm}$ [5,6]. The absence of a visible hysteresis loop, initially interpreted as a signature of a second-order transition, is more likely due to increased thermal fluctuations reducing the size of the hysteretic effect as T_{MI} is shifted to higher temperatures. Indeed, measurements performed on YNiO$_3$[21] and SmNiO$_3$[33] detected a small but visible hysteresis of the resistivity versus temperature curve close to the critical temperature.[21] On the other hand, the Néel transition is observed to be first-order for the compounds displaying $T_{Néel} = T_{MI}$ and second-order in those for which $T_{Néel} < T_{MI}$ [33-35]. A paramagnetic metallic behavior has always been observed for bulk polycrystalline LaNiO$_3$ samples, at all probed temperatures [5,6,36]. Nevertheless, measurements on recently synthesized LaNiO$_3$ single-crystals have suggested a surprising antiferromagnetic transition at $T_{Néel}$ = 157 K, while the material remains metallic and rhombohedral [37,38].

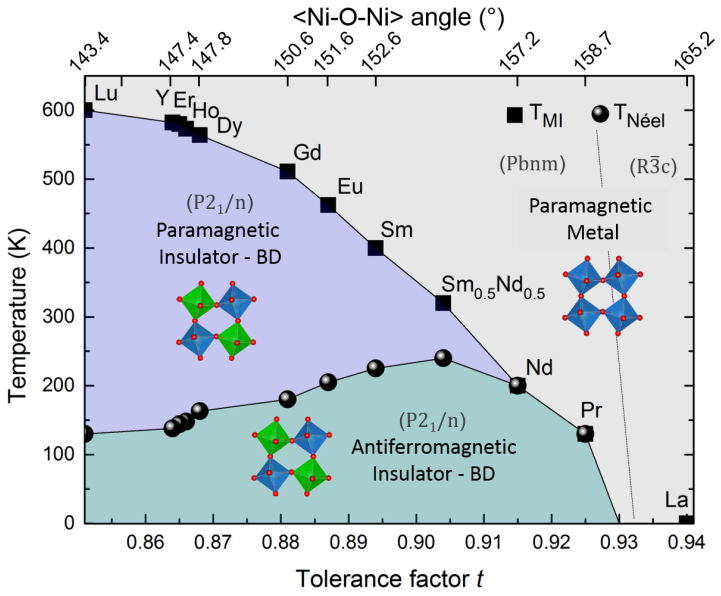

Figure 4: Phase diagram of the RNiO$_3$ family summarizing the evolution of the structure as well as the metal-insulator and Néel transition temperatures as a function of the tolerance factor t (bottom x axis) and the <Ni-O-Ni> angle Θ (top x axis). BD indicates the bond-disproportionated state. $R\bar{3}c$, *Pbnm* and $P2_1/n$ indicate space groups corresponding to rhombohedral, orthorhombic and monoclinic crystal structures, respectively. A sketch of the high and low temperature structure is overlaid on the figure. Notice that the scale of the <Ni-O-Ni> angle is non-linear. The t values are calculated from experimental measurements of the R-O and Ni-O distances and therefore differ from the theoretical ones, which assume a purely ionic bonding. Adapted from ref [6,20,22,39].

3.2 Basic electronic configuration

If we assume that the Ni-O bonds are perfectly ionic and that the NiO$_6$ octahedra are perfectly regular, the nominal Ni valence state should be Ni^{3+} with the Ni sites hosting 7 electrons in the d orbitals, resulting in the d^7 low spin configuration $t_{2g}^6 e_g^1$. Thus, neglecting the crystal field produced by the orthorhombic distortion, the two e_g orbitals, $x^2 - y^2$and $3z^2 - r^2$, should be equally occupied. Despite the nominal picture, RNiO$_3$ compounds are characterized by a small charge transfer energy Δ [16,40], which facilitates the relocation of electrons from the p oxygen band to the Ni d states, corresponding to the electronic configuration d^8L, where L indicates a hole in the oxygen band. Then, the effective RNiO$_3$ ground state would be more adequately described as a mixed configuration $\alpha d^7 + \beta d^8 L$ [41,42]. In principle, the nominal d^7 configuration should favor a Jahn-Teller distortion and the stabilization of an orbital superstructure, in order to remove the degeneracy of the e_g orbitals [34,35,41]. However, experiments indicate the absence of orbital ordering in the RNiO$_3$ family [35,43,44]. Instead, several spectroscopy studies performed at liquid nitrogen temperature (80 K) point toward the predominance of the d^8L configuration in determining the relevant properties of these compounds, consistent with a vanishing charge transfer energy, Δ [17,18,41,45]. In fact, both

calculations and experimental results confirm that Δ can be small or even negative for the RNiO$_3$ compounds, with a dominant contribution of the d^8L electronic configuration [26,46]. Recent experiments combining x-ray absorption (XAS) and resonant inelastic x-ray scattering (RIXS) show that the oxygen *p*-band contributes significantly to the RNiO$_3$ electronic structure, confirming the negative charge transfer scenario [46]. This spontaneous occurrence of oxygen holes in the nickelates is sometimes referred to as self-doping.

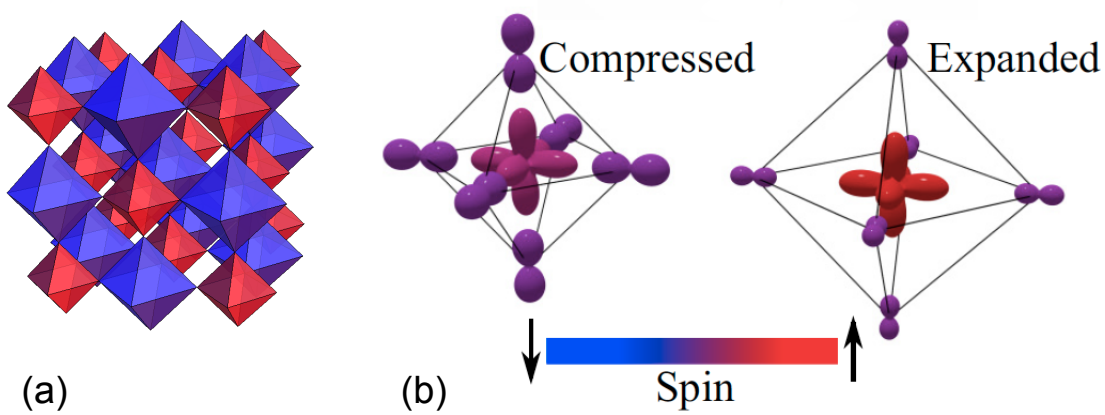

Figure 5: Illustration of the BD characterizing the ***R*NiO$_3$** ground-state. (a) The short-bond NiO$_6$ units surrounded by long bond NiO$_6$ units, forming a checkerboard arrangement. (b) Sketch of the electronic configuration corresponding to the two inequivalent Ni sites, highlighting the charge and spin distribution. Adapted from ref. [32]

Concerning the metallic phase, the Fermi surface of the nickelates is formed by an electron pocket at the Γ point and hole pockets centered at the corners of the Brillouin zone, giving two distinct conduction channels [47-50]. In fact, the Hall coefficient of the nickelates is positive, indicating the presence of *p*-carrier, whereas measurements of the Seebeck coefficient reveal mainly *n*-carriers [51-58]. Thus, a correct model of the metallic phase should take into account at least two conduction bands.

3.3 Metal-to-Insulator Transition (MIT)

Perhaps the most fascinating property of the rare earth nickelates is their MIT, the nature of which has been heavily studied for over twenty years. This MIT, which is appealing application-wise, stands as a textbook example of a bandwidth-controlled transition [59]. The MIT occurs at a temperature (T_{MI}) that is related to the degree of orthorhombic distortion throughout the family. As the distortion increases and the Ni-O-Ni angle Θ decreases from 180º, the *d-p* orbital overlap and,

therefore, the hopping strength t_{pd} are reduced. Consequently, the bandwidth W of the system decreases and T_{MI} rises from 0 K ($LaNiO_3$) up to 600 K ($LuNiO_3$) [60].

The observation of a significant ^{16}O-^{18}O isotope effect on T_{MI} highlighted the presence of a marked electron-lattice coupling in the system and its substantial role in the MIT.[61] In fact, as described in section 3.1, the MIT is concomitant with a symmetry reduction to a monoclinic structure, accompanied by a breathing distortion of the NiO_6 octahedra, creating two inequivalent Ni sites in the insulating phase. Such a breathing distortion, which leads to a bond-disproportionate state with long and short Ni—O bonds (see Fig. 5), lowers the symmetry and is a key ingredient for the stabilization of the RNiO$_3$ insulating ground state.

Initially, the bond disproportionation was associated with a charge ordering on the Ni sites, alternating $d^{7-\delta}$ and $d^{7+\delta}$electronic configurations [21,44,62]. Such a scenario was reinforced by a variety of experimental measurements: resonant x-ray diffraction at the Ni K-edge [62], high resolution neutron and non-resonant x-ray diffraction [23,24], high resolution x-ray absorption spectroscopy (XAS) [63] and, more recently, ^{57}Fe probe Mössbauer spectroscopy [64]. The presence of the charge disproportionation was inferred either from analysis of the diffraction patterns, which revealed bond lengths corresponding to the two inequivalent Ni sites (Brown bond-valence model [24]) or, alternatively, a valence splitting of the Ni cations was extracted from high resolution XAS at the Ni K-edge [63]. Interestingly, these studies also show that the amount of charge disproportionation, δ, increases with the degree of orthorhombic distortion along the family [24,63]. Most recent calculations and experiments, however, support a more subtle picture in which a uniform Ni d^8 occupation is more likely to occur. According to this picture, the configuration in the high temperature, metallic phase would be close to d^8L for all Ni atoms and then, as the bond disproportionation distortion takes place, there would be a splitting $d^8L + d^8L \rightarrow d^8L^2 + d^8$ into two different Ni sites [25-28,41]. The Ni-d^8 state corresponds to the Ni atoms in the large O_6 octahedral cages and can be described as a Ni^{2+} cation in a high-spin state ($t_{2g}^6 e_{g\uparrow}^2 e_{g\downarrow}^0$ configuration with S = 1). Regarding the Ni-d^8L^2 ion, located within the small O_6 octahedron, it also resembles a Ni^{2+} ionization state and a direct estimate of charge transfer between the two Ni sites, using DFT+U calculations, renders a negligible result [25,28,65]. Despite this, however, the two Ni states are in fact very different: the Ni-d^8L^2 ion has a fully occupied t_{2g}^6 shell (as it would correspond to a Ni^{4+} low-spin configuration) and, additionally, it shares about two electrons (ligand holes) from the surrounding oxygen octahedron. These additional electrons are not (or, at most, weakly) spin polarized, so that the total magnetic moment of this Ni is nearly null (in good approximation, we have an S = 0 spin configuration). Thus, the insulating gap splits the dispersive d^8L band of the high temperature phase into two localized bands [18,25-27].

It is interesting to note that the above picture for the ground state of the RNiO$_3$ compounds has now been verified by various model-Hamiltonian, DMFT+DFT and DFT+U approaches, all of which render compatible results [25-28]. We will discuss the theoretical efforts further in Section 3.7.

3.4 Néel transition

For $T < T_{Néel}$, the insulating phase of the nickelates becomes antiferromagnetically ordered. The antiferromagnetic arrangement is characterized by the wavevector $q_0 = (¼, ¼, ¼)_{pc}$ in the pseudocubic notation (or by $q_0 = (½, 0, ½)_o$ in orthorhombic notation), which indicates a periodicity of 4 monolayers along the $(111)_{pc}$ (or $(101)_o$) crystallographic direction [66]. Typically, the rare earth sublattice also tends to stabilize an antiferromagnetic structure characterized by the same Bragg vector $q_0 = (¼, ¼, ¼)_{pc}$. The existence of this antiferromagnetic order has been probed with both neutron and resonant soft x-ray diffraction measurements: for example, Fig. 6a shows a sharp Bragg peak corresponding to $q_0 = (¼, ¼, ¼)_{pc}$ as measured with linearly polarized soft x-rays at the Ni L_3 resonance of a SmNiO$_3$ film. In particular, the temperature dependence of the antiferromagnetic structure was studied with x-rays, tuned resonantly to both the Ni L- and rare earth M- edges, in order to distinguish the individual contributions of the Ni and rare earth cations, as illustrated in Fig. 6b. Looking at the temperature evolution of the magnetization of the Ni sublattice suggests a second-order transition for compounds with $T_{Néel} < T_{MI}$, whereas an abrupt, first order, change is observed for those with $T_{Néel} = T_{MI}$ [67]. On the other hand, the magnetic order of the R-sublattice is induced by the magnetic order of the Ni-lattice, as confirmed by the observation that the R-cation magnetization rises gradually as the temperature is reduced below $T_{Néel}$ [36,68,69].

The knowledge of the exact magnetic structure has been hindered for many years by a lack of experimental data on bulk samples. Neutron powder diffraction experiments performed by García-Muñoz *et al.* suggested that the Bragg vector should correspond to an up-up-down-down sequence of the Ni moments along the $(111)_{pc}$ direction, accompanied by an orbital superlattice.[66] Yet, the experimentally measured magnetic structures of bulk compounds are compatible with both collinear and non-collinear models. While high quality data on nickelate single crystals may still shed new light on this issue, resonant soft x-ray diffraction measurements performed by Scagnoli *et al.* on NdNiO$_3$ thin films ruled out the existence of orbital-ordering, demonstrating that the magnetic structure can be described by a non-collinear spin density wave [43]. Following this, the non-collinear antiferromagnetic structure was also observed in some of the other members of the nickelate family while no direct evidence of the existence of a collinear structure has been reported so far in any RNiO$_3$ film [70,71]. A sketch of the non-collinear spin structure is illustrated in Fig. 6c.

As previously described, looking at the bulk $RNiO_3$ phase diagram (Fig. 4) one can distinguish two main regimes, one for which $T_{Néel} = T_{MI}$ and a second where $T_{Néel} < T_{MI}$. Originally, it was suggested that such a difference in the critical temperature of the system could be related to the existence of distinct electronic correlations for the members with $r_A < r_{Nd}$, changing the intrinsic nature of the insulating ground state [67,72]. Furthermore, Lee *et al.* proposed a Landau model for *R* = Nd, Pr where both the MIT and Néel transitions result from the nesting of a spin density wave at $q_{Bragg} = (\ ¼\ ¼\ ¼\ )_{pc}$, suggesting that the antiferromagnetic interaction drives the MIT, in agreement with Medarde *et al.* [50,61]. In spite of these interesting proposals, for the case of bulk nickelates with R ≠ La the experimental results confirm that the antiferromagnetic phase can be stabilized only below ($T_{Néel} < T_{MI}$) or concurrently with ($T_{Néel} = T_{MI}$) the MIT, suggesting that the magnetic interaction is suppressed by charge fluctuations in the presence of delocalized electrons [5,6].

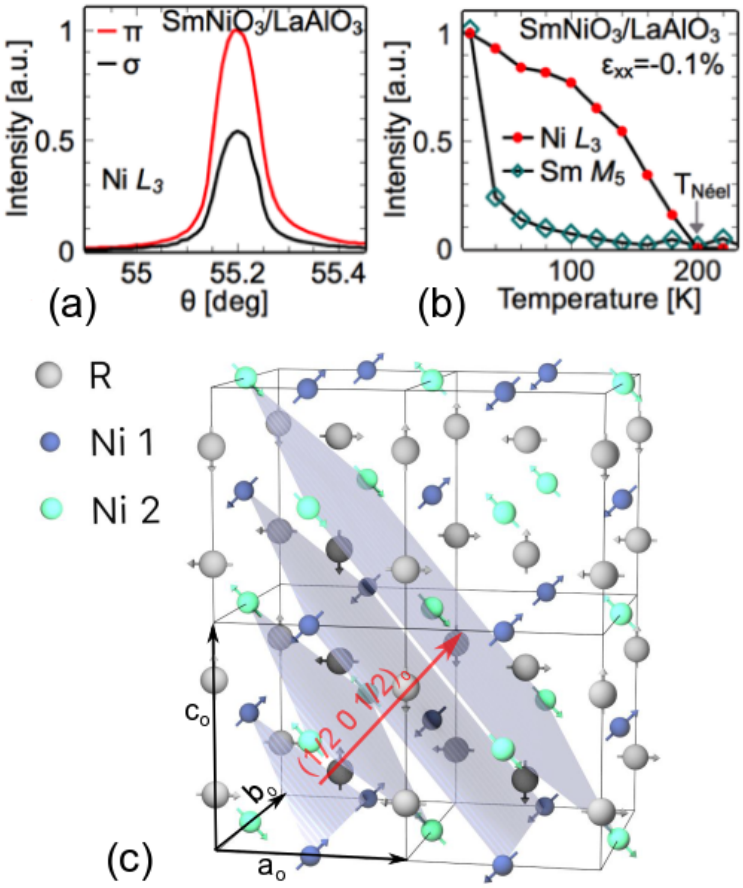

Figure 6: (a) Bragg peak corresponding to the $(¼\ ¼\ ¼)_{pc}$ wavevector of a $SmNiO_3$ film (10 nm), measured with resonant soft x-ray scattering at the Ni L_3 edge, with π (red curve) and σ (black curve) polarized light, at T = 4 K. The linear dichroism is consistent with the antiferromagnetic nature of the diffracted intensity. (b) Temperature dependence of the intensity of the $(¼\ ¼\ ¼)_{pc}$ Bragg peak, measured at the Ni L_3 and Sm M_5 resonances of the same $SmNiO_3$ film, showing the induced behavior of the magnetization at the rare earth edge. (c) Sketch of a proposed non-collinear magnetic structure for the nickelates. The black arrows indicate

the axes of the *orthorhombic* unit cell. The red arrow highlights the Bragg vector $(½\ 0\ ½)_o$ in *orthorhombic* notation, which corresponds to $q_0 = (¼\ ¼\ ¼)_{pc}$ in *pseudocubic* notation.

Within this picture, the case where $T_{Néel} = T_{MI}$ would not indicate a particular coupling between magnetic and charge interactions, but would simply result from the quenching of the Néel transition down to T_{MI}. Such a picture is also supported by recent theoretical calculations[73] and optical spectroscopy experiments [74]. Lu *et al*. have studied the charge and spin response functions of RNiO$_3$ with multiorbital random phase approximation (RPA) in a two-band Hubbard model, showing that a charge instability at the wave vector $q_c = (½\ ½\ ½)_{pc}$ drives the system into the bond-disproportionated phase via strong electron-phonon coupling, whereas the spin instability at $q_{Bragg} = (¼\ ¼\ ¼)_{pc}$ plays only a minor role in the MIT [73], contrary to the proposal of Lee *et al*. Moreover, Ruppen *et al*. have measured the temperature dependence of the optical conductivity spectra of epitaxial films within a regime that reproduces the RNiO$_3$ bulk behavior well [74]. In this work, the authors demonstrate that the onset of the antiferromagnetic order only reinforces the bond-disproportionation, while the MIT remains bound to the onset of breathing distortion, which is identified as a vital ingredient for the MIT to occur [74]. Similar conclusions are reached in recent DFT+U works [27,73].

While these conclusions are currently well-established for the case of polycrystalline bulk samples and sufficiently thick (above 10 u.c.) films of nickelates, ultrathin films and nickelate-based superlattices reveal an even richer behavior, as described in detail in the following sections. Also, as mentioned in section 3.1, the growth of high quality LaNiO$_3$ single crystals has been recently reported, together with the observation of static magnetic ordering within the metallic phase [37,38]. Such results may mean that, in the coming years, the so-far well-established nickelate phase diagram may need to be modified to reflect these new perspectives,.

3.5 Behavior under pressure

The nickelate phase diagram is controlled by the degree of orthorhombic distortion of the system, which in turn governs the orbital overlap. For the bulk members, this distortion is linked to the tolerance factor, *t*, which varies across the family with the *R* cation size. Alternatively, the effective structural distortion characterizing each member can be modified by the application of hydrostatic pressure. The electronic properties of bulk nickelates subject to different levels of pressure were investigated in depth in the early 90s. Obradors *et al.*[75] and Canfield *et al.*[76] studied the MIT for the cases of NdNiO$_3$, PrNiO$_3$ and the mixed solution $Nd_{0.7}La_{0.3}NiO_3$, under pressures ranging from 1 bar to 30 kbar (= 3 GPa). Later on, similar pressure measurements were performed on more distorted members of the family, such as SmNiO$_3$ [77] and YNiO$_3$ [78,79]. In all investigated cases,

increasing the applied pressure results in a decrease of the transition temperature T_{MI}, whereas the room temperature resistivity of the samples remains unchanged. For the case of $PrNiO_3$, the insulating phase is suppressed for sufficiently high pressure (P > 11.6 kbar), metallic transport behavior being observed throughout the whole temperature range probed (4 K – 300 K). For the case of $NdNiO_3$, the suppression of the metallic phase was predicted to occur for P > 31 kbar, which exceeded the maximum pressure attainable during the experiments [75]. Notably, such a behavior distinguishes the nickelates from other charge transfer oxides, e.g. the layered cuprates, for which the insulating phase is stabilized by the application of increasing hydrostatic pressure [75,80].

The closing of the insulating gap E_{gap} with pressure can be explained by an increase of the system bandwidth (*W*) associated with the imposed structural constraints [28,81]. Roughly speaking, E_{gap} depends on the difference between the charge transfer energy Δ and the system bandwidth W: E_{gap} = Δ – W. In the $R NiO_3$ family, the corner-sharing NiO_6 octahedral units tilt in order to adapt to the difference between the *R*-O and Ni-O bond lengths, as quantified by the tolerance factor, *t*. The application of pressure helps to reduce such a mismatch by diminishing the empty space in the unit cell, so the system tends to have smaller orthorhombic tilts, or, equivalently, straighter Ni-O-Ni bond angles, as experimentally observed by Medarde *et al*. in bulk $PrNiO_3$ compounds [82]. As a consequence, the overlap of the oxygen band with the Ni *d*-shell increases and the bandwidth broadens, favoring conductivity. On the other hand, the charge transfer energy Δ seems to be essentially unaffected by pressure[75,83], in contrast with the case of other charge transfer compounds such as the layered cuprates. Finally, x-ray absorption spectroscopy (XAS) measurements performed by Ramos *et al.* on $YNiO_3$ indicate that, within the resolution of the experiment, the local geometry of the NiO_6 units remains unaffected by pressure [79].

3.6 Behavior under magnetic field, multiferroic effects

Few studies have been published concerning the effect of magnetic field on the $R NiO_3$ properties. Yet, Canfield *et al.* reported that the resistivity curves and T_{MI} of $NdNiO_3$ are, in essence, insensitive to the application of fields of up to 4 T[76], suggesting that the $R NiO_3$ behavior is extremely robust against magnetic field, which, in turn, suggests magnetoresistive effects should be small.

In this context, it is worth noting that an improper ferroelectric order in the insulating phase of the nickelates, driven by the onset of the Ni spin order, which would break the $P2_1/n$ centrosymmetry to render the material polar, has been predicted from DFT+U simulations [84]. Such a magnetically-induced electric polarization should thus be highly responsive to changes in the spin

configuration, as is typical of the so-called "type II" multiferroics (such as e.g. $TbMnO_3$), which show similar behavior [85,86]. If such a polar order were experimentally confirmed, its control by means of magnetic fields would open yet another interesting field of possibilities for RNiO$_3$ compounds.

3.7 Theory and predictions

The theoretical work on nickelates has proved challenging, as only recently a consensus has been reached on the nature of the insulating phase of these compounds. It is not our purpose here to give a detailed account of the evolution of the theory of nickelates. We will limit ourselves to summarizing the current status of the field, and to comment briefly on the relative position of the model-Hamiltonian and first-principles simulation approaches to these materials.

The most common approach to studying nickelates, or any strongly correlated oxide for that matter, starts with the formulation of model Hamiltonians, which are then solved analytically or numerically. The numerical solutions range from exact diagonalization for small clusters, to approaches combining dynamical mean field theory (DMFT) and density functional theory (DFT) techniques, which permit a better embedding of the part of the system that is treated more accurately. Such numerical techniques are characterized by providing a good description of exchange and correlation effects in the many-body electronic problem. Thus, the critical step in the model-Hamiltonian approach is the definition of the model itself and the determination of its parameters, a task that is far from trivial in the case of nickelates.

Today we know that a successful model for the insulating nickelates must account for the possible formation of holes in the ligand anions; it must also effectively incorporate the effects of a breathing distortion of the O_6 octahedra as an important, or even necessary, condition for the insulating state to emerge. The relevance of these factors was summarized by Park *et al.* [25], whose models (including the t_{2g} and e_g Ni orbitals in the DMFT basis set and solving by DFT+DMFT methods) capture the insulating state of these compounds, the differentiated magnetic and electronic behavior of the two Ni sites (termed "site-selective Mott transition" by these authors), and the enigmatic absence of charge order. More recently, Johnston *et al.* [26] worked with a model-Hamiltonian for Ni e_g and O p orbitals, which they solved for small clusters of atoms by exact diagonalization. In agreement with Park *et al*., these authors showed that the insulating state of the nickelates is associated with two distinct Ni sites with $(d^8L^2)_{S=0}$ and $(d^8)_{S=1}$ configurations, which

they described as "charge ordering without actual movement of the charge". Finally, other relevant modeling studies were performed by Subedi *et al.* [27] and, more recently, Seth *et al.* [87], who showed that a minimal (low energy) Hamiltonian including only the Ni e_g bands and solved via DFT+DMFT methods was sufficient to capture the insulating ground state of these materials for a wide range of input parameters. The work of Subedi *et al.* [27] emphasizes the importance of the breathing (monoclinic) distortion of the structure, as this causes a modulation of the effective on-site energy of the e_g orbitals, which, in turn, favors the differentiated behavior of the two Ni sublattices. Further, in their original work [27] and in a later analysis of experimental optical spectra [88], Ruppen *et al.* find evidence that a better description of the nickelates may be achieved for relatively small values of the Coulomb repulsion U (~ 1-2 eV), which comes close to the Hund's coupling constant J (~ 0.8 eV).

Hence, while there are open issues on the model Hamiltonian front, for example, regarding the description of the experimentally-observed spin order, it seems fair to say that the basic picture of the insulating nickelates is finally well-established. It is interesting to note that, in hindsight, many of the ingredients in the final (correct) solution were already present in the early theoretical study of Mizokawa *et al.* [41], although that work seemed to imply an actual transfer of charge between the Ni sites, the absence of which has caused considerable confusion over the years.

Among other materials, rare earth nickelates have a peculiarity that makes them very challenging for traditional model-Hamiltonian studies, namely, the critical role that structural distortions play in the stabilization of the insulating phase. The importance of some atomistic features, in particular the concerted rotations of the NiO_6 octahedra, is apparent from the nickelate phase diagram. However, the importance of the octahedral breathing was not so easy to grasp *a priori* in the context of strongly correlated oxides, in which structural distortions, such as Jahn-Teller, can typically be assumed to *follow* an electronic driving force. Realizing that such structural features are so important, and incorporating their effects into the electronic Hamiltonians, has been crucial to achieve a satisfactory description of these compounds.

The challenges posed by rare earth nickelates highlight the usefulness of first-principles approaches that, like DFT, provide a complete, structural and electronic, self-consistent description of the material. In fact, the major theoretical works mentioned above[25,27] rely on a systematic application of DFT methods to define and compute the parameters of the corresponding model Hamiltonians. Extending the theoretical work on nickelates toward the design and optimization of new materials will lean heavily on the performance of DFT-based methods, such as the Hubbard-corrected "DFT+U", that will allow the structural and electronic ground state of hypothetical

systems to be solved in an unbiased way. Fortunately, our understanding of how to treat nickelates at the DFT+U level has improved very much over the past few years, to the point where these methods now offer a standalone alternative to the investigation of these compounds.

Indeed, systematic DFT+U investigations of rare earth nickelates have shown that these methods capture the splitting of the Ni sites into $(d^8L^2)_{S=0}$ and $(d^8)_{S=1}$ sublattices in a natural and self-consistent way [28], producing quantitatively correct results for all measured structural and magnetic properties [28,29,89] and, most recently, offering new insights into the triggered nature of the MIT [89]. For years, one of the few lingering issues with DFT+U methods has been the prediction that the ground state of these compounds is ferromagnetically ordered [29]; however, recently it was realized that this result is strongly dependent on the U_{eff} correction used in the simulations [31]. More precisely, if large U_{eff} values (~ 7eV) are used, a collinear ferromagnetic solution is indeed favored; however, if relatively small U_{eff} values (< 2eV) are used instead, a collinear antiferromagnetic ground state is stabilized [28,89]. Further, the results of Prosandeev *et al.* [29] suggest that a similar U-dependence is observed when allowing for non-collinear spin structures in the simulations. Hence, while we still lack a detailed study finally settling this issue, the existing results indicate that DFT+U simulations with a small U correction are able to correctly predict the basic features of the non-collinear magnetic structure of nickelates.

It is interesting to note that the comparison of DFT+U and experimental results suggests that nickelates are better treated by using small values of the effective Hubbard U_{eff} parameter, which, in the most common approach [90], can be interpreted as the difference $U_{eff} = U - J$. This is in agreement with the conclusions of the aforementioned Ref. [88], which used model Hamiltonians to interpret measured optical spectra. Further, noting that the choice of U_{eff} in DFT+U simulations determines all the computed properties – structural, electronic, magnetic –, and that the agreement with experiment is good for all of them [28,89], we can be optimistic about the robustness and reliability of current DFT+U simulations of these materials.

Let us also point out that, while DFT+U simulations do not incorporate statistical averages by default, it is perfectly possible to use these schemes within e.g. molecular dynamics [91] or time-dependent DFT [92] frameworks and access the temperature-dependent behavior of the material. An application of such methods to nickelates, including the possibility that spins disorder, would be computationally intensive, but perfectly viable as a matter of principle. In fact, recent DFT+U results suggest that this would be a promising strategy to elucidate the conditions for the simultaneous, or separated, MIT and spin-ordering transitions. Note that Varignon *et al.* [28] have

shown, using DFT+U methods, that the bulk RNiO$_3$ compounds with R = Lu-Sm support an insulating state irrespective of the spin order, a result that is compatible with the existence of a spin-disordered insulating phase for those materials. In contrast, the same authors predict that bulk NdNiO$_3$ and bulk PrNiO$_3$ would be metallic if their spins were to adopt a ferromagnetic arrangement. It thus follows that, when in a magnetically disordered state, with spins dynamically exploring all sorts of locally antiferromagnetic (insulating) and ferromagnetic (metallic) configurations, such compounds will appear to be metals. This is consistent with the experimental observations for bulk nickelates, and suggests that DFT+U simulations correctly capture the effects behind the temperature-driven transitions in the family.

Interestingly, as we will see below, it is experimentally known that epitaxial effects in NdNiO$_3$ films can induce an insulating paramagnetic state not accessible in the bulk material [93]. This suggests that a DFT+U calculation should predict such NdNiO$_3$ films to be insulating irrespective of the spin order, a conjecture that remains to be tested. Predictably, in the near future, we will see a growing number of DFT+U simulations of nickelate heterostructures; this will hopefully confirm that these methods retain the accuracy obtained for the bulk compounds, and are thus useful to understand and design evermore complex materials.

Let us note that our current picture for the insulating phase of the rare earth nickelates was already hinted at in early DFT+U works. For example, in 2002 Yamamoto and Fujiwara[94] investigated YNiO$_3$ and reported the ground state that is commonly accepted today. Interestingly, in agreement with most (if not all) DFT+U publications in the literature, these authors observed that the computed charge difference between Ni sites is negligible, a result that may have seemed in conflict with experiments and model theories in the past, but which we now know is perfectly correct. The same ground state was obtained and further analyzed by Mazin *et al.*[44] who emphasized that the coexistence of two distinct Ni sublattices provides a mechanism for the MIT of nickelates and explains the absence of on-site Jahn-Teller distortions. It is also relevant to mention here the work that Raebiger *et al*.[95] published in 2008 on how charge orders upon changing the nominal oxidation state of transition metal atoms. These authors explained a widespread DFT finding – that "calculations show only negligible changes in the local transition metal charge as the oxidation state is altered" – in terms of a "negative charge-feedback" mechanism, which they illustrated with various examples. In absence of a detailed investigation, it does seem that the alleged charge order of rare earth nickelates follows the "negative charge-feedback" rules, as proposed in Ref. [95].

In summary, the MIT in RNiO$_3$ nickelates has been studied in great detail by a variety of theoretical and quantum simulation approaches, all of which have by now converged to a common picture of the physical mechanism behind it with a key role played by the bond disproportionation. Hence, theory-wise, we are now well-equipped to tackle the RNiO$_3$-based heterostructures of great interest today.

4. RNiO$_3$ THIN FILMS

4.0 Motivation

While the first successful synthesis of bulk RNiO$_3$s was demonstrated in 1971 by Demazeau *et al.* [96], their physical properties were extensively characterized only in the early 90s in the pioneering work of García-Muñoz *et al*. [34,36,66] The discovery of a distinctive MIT in all members of the family, excluding the case of R = La, and the observation of a peculiar antiferromagnetic structure characterizing the insulating phase, sparked interest in the compounds. Nonetheless, the experimental study of nickelates was limited to polycrystalline ceramic samples, the single crystal size being restricted to the micron scale. Furthermore, the synthesis of the materials involved challenging conditions, requiring both extremely high oxygen pressure and high temperature for the chemical stabilization of the perovskite phase. While the synthesis of high quality LaNiO$_3$ single crystals has recently been reported [37,38], achieving high quality nickelate samples in thin film form has so far been essential for the experimental study of these compounds.

Nowadays, thin film deposition techniques, such as molecular beam epitaxy (MBE), pulsed laser deposition (PLD) and radio-frequency off-axis magnetron sputtering, yield highly crystalline RNiO$_3$ thin films and enable advanced atomic-scale control of their lattice and electronic properties.

With respect to the bulk counterparts, the behavior of thin films can be highly sensitive to the choice of substrate, dimensionality and the possibility of combining together different compounds into a superlattice structure.[1] In the following, we attempt to cover the plethora of experimental and theoretical work that applies such a strategy to the RNiO$_3$ family.

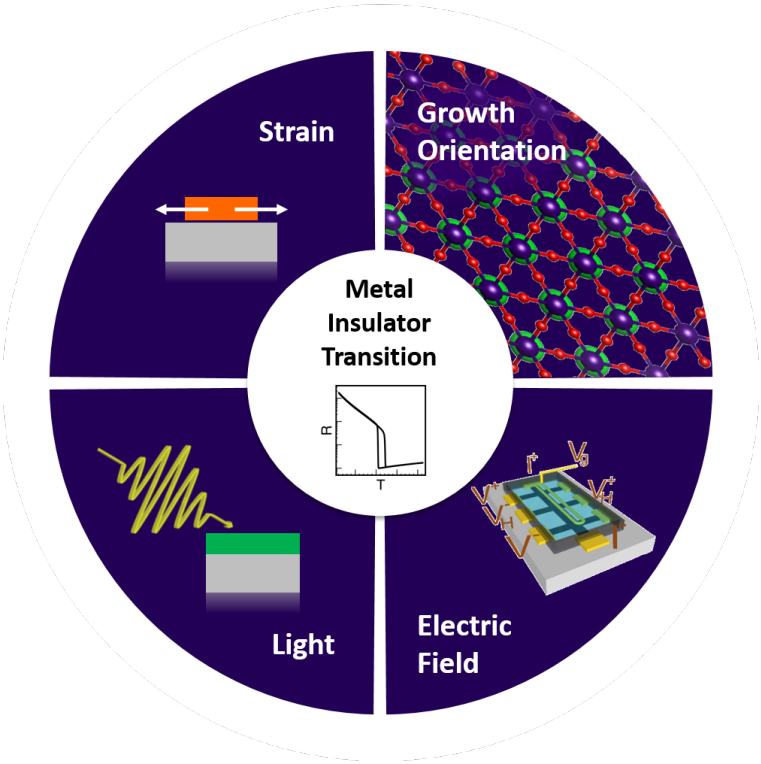

Figure 7: Strategies to tune the metal-to-insulator transition in RNiO$_3$ thin films.

4.1 Control of the Metal-to-Insulator Transition

4.1.1. Strain Engineering on $(001)_{pc}$-oriented films

The structure of nickelates can be modified by growing epitaxial films on top of different substrates, providing varying levels of epitaxial strain (ε_{xx}). Since the in-plane lattice parameter of the film has to match the lattice structure of the substrate, the film will experience, with respect to its bulk counterpart, an in-plane biaxial strain constraint ε_{xx}, defined as:

$$\varepsilon_{xx} = \frac{a_{sub} - a_{bulk}}{a_{bulk}}$$

where a_{bulk} is the in-plane lattice parameter of the film material in its bulk form and a_{sub} is the in-plane lattice parameter of the substrate. Due to this in-plane constraint, the out-of-plane lattice

parameter of the film will expand (compressive strain) or contract (tensile strain) in order to reduce the volume change, resulting in a tetragonal distortion of films grown along the $(001)_{pc}$ crystallographic axis. Consequently, the BO_6 units composing the perovskite structure have two main structural pathways in order to accommodate such a distortion in epitaxially coherent heterostructures: The oxygen octahedra can either adopt a Jahn-Teller distortion (i.e. elongate in-plane (out-of-plane) in response to tensile (compressive) strain and, consequently, stabilize the occupation of the in-plane (out-of-plane) –oriented orbitals) or, alternatively, arrange themselves into a lower symmetry rotation pattern, often promoting a more distorted B-O-B bond angle [11].

For the case of the nickelates, epitaxial strain is a widely investigated strategy to control their functionalities and has been proved to be very efficient in this respect. Much research effort has been spent on strain engineering for achieving orbital polarization of e_g orbitals. For this purpose, most of the experimental work has focused on $LaNiO_3$, as described in section 4.2. Epitaxial strain has also been heavily researched in the other members of the family as a way to tune the electronic transitions. In this case, the applied epitaxial strain provides a fine control of the MIT over temperature [69,97-106]. As an example, Fig. 8a displays the resistance as a function of temperature of $NdNiO_3$ films grown on top of $(001)_{pc}$-oriented perovskite substrates providing different levels of biaxial strain. As ε_{xx} ranges from the tensile regime to the compressive regime, the film T_{MI} is gradually shifted to lower temperatures and, eventually, a single metallic phase is stabilized for sufficiently high compressive strain. Furthermore, in all cases, even for effectively no strain, the observed MIT occurs at temperatures below the bulk transition temperature (see Fig. 8c). This transport behavior has been reported by several groups and observed for different RNiO$_3$ compounds, indicating that a common mechanism intervenes in response to epitaxial strain [69,105].

Similar to the case of bulk nickelates subject to hydrostatic pressure described previously, the lowering of T_{MI} with compressive strain points to a bandwidth broadening driven by the applied structural constraints. The relation between epitaxial strain and bandwidth change is well captured by DFT calculations. As presented in Fig. 8b, a monotonic broadening of the system bandwidth W with strain is driven by a corresponding straightening of the Ni-O-Ni angle out-of-plane, accompanied by the stretching (squeezing) of the out-of-plane (in-plane) Ni-O bond length.

Thus, the RNiO$_3$ lattice responds to epitaxial strain by modifying the degree of distortion characterizing the system. These observations are summarized in Fig. 8c, which shows the evolution of the electronic transitions of $SmNiO_3$ and $NdNiO_3$ as a function of strain, compared to the phase diagram of bulk RNiO$_3$ parameterized by the tolerance factor. Clearly, the effect of compressive strain on the MI and Néel transitions is equivalent to a change of the R cation size, or, equivalently, to a shift of the tolerance factor of the system. In contrast, increasing epitaxial tensile

strain applied in the $(001)_{pc}$ crystallographic plane does not result in an increase of T_{MI}, as the temperature of the MIT saturates lower than in the corresponding bulk nickelate. This observation leads to two basic conclusions: First, thin films of nickelates grown epitaxially along the $(001)_{pc}$ direction always stabilize a less-distorted Ni-O-Ni angle, with respect to their bulk counterparts, indicating that the presence of the $(001)_{pc}$-oriented perovskite substrate matrix alone promotes a systematic change of the effective chemical pressure on the RNiO$_3$ lattice; Second, as the strain becomes more tensile, the lattice does not accommodate strain with a stronger orthorhombic distortion. In fact, the transport measurements of RNiO$_3$ films under tensile strain show that the resistivity of the system increases for high levels of tensile strain ($\varepsilon_{xx} \geq 3\%$), suggesting that the elastic energy cost for deforming the film lattice exceeds the formation energy of structural defects, such as vacancies or dislocations, as discussed by Conchon and coworkers [107].

An alternative perspective has recently been proposed by Zhang *et al.*, who suggested that the occurring of the MIT may be intimately linked to symmetry. They showed that the MIT is suppressed in NdNiO$_3$/YAlO$_3$ thin films, in which the epitaxial strain imposes the $P2_1/m$ structure that does not allow the structural transition to the monoclinic $P2_1/n$ space group associated with the bond-disproportionation [108].

Finally, Mikheev *et al.* have proposed an original phase diagram for NdNiO$_3$ thin films, adopting epitaxial strain and thickness as control parameters that drive the system from the paramagnetic metallic to the antiferromagnetic insulating phase [109]. In particular, the authors have shown that the metallic regime can be described either as a non-Fermi liquid (NFL) or a Landau Fermi liquid (LFL) depending on the thickness of the films and the applied strain, which tune, respectively, the degree of disorder in the system and the amount of orbital polarization of the e_g levels.

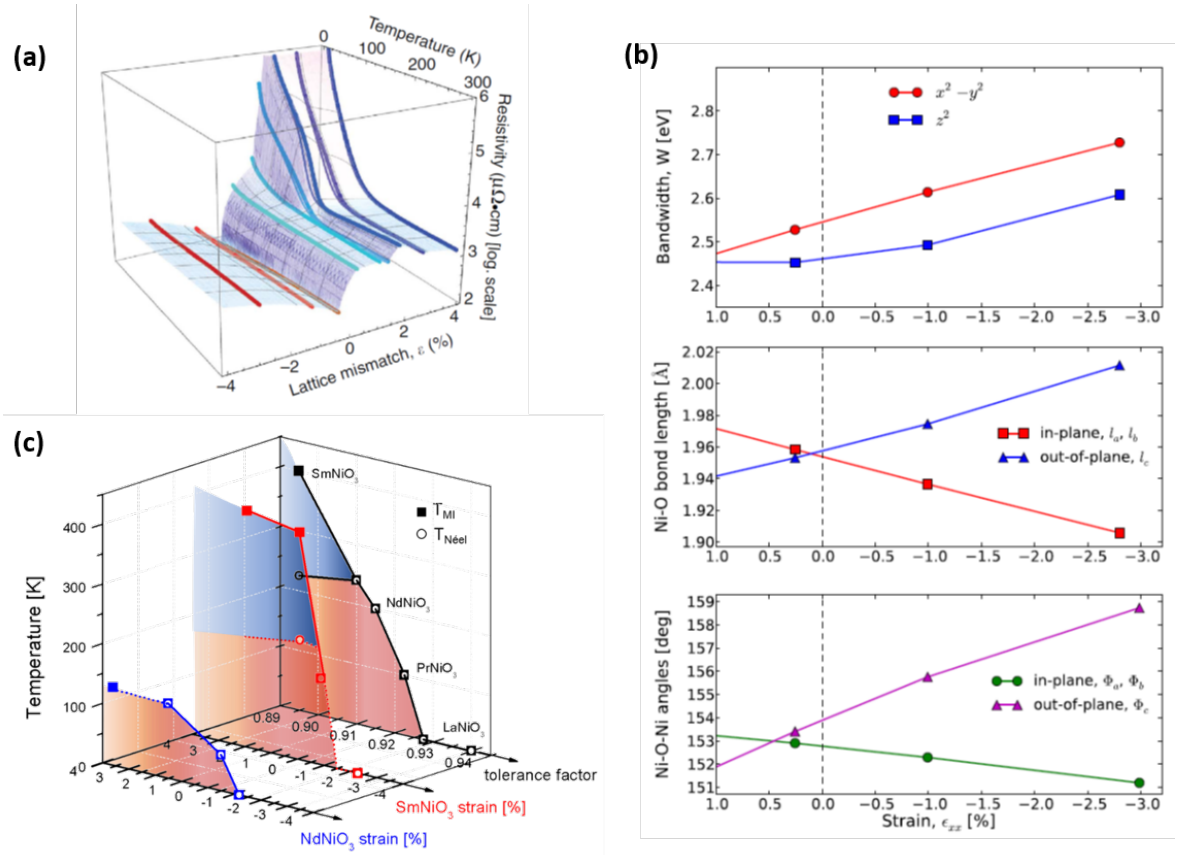

Figure 8: Tuning of the electronic properties of the perovskite nickelates by epitaxial strain. (a) Temperature- and lattice mismatch-dependence of the resistivity of $(001)_{pc}$-oriented $NdNiO_3$ films. Adapted from Ref. [101]. (b) DFT calculations showing the strain-dependence, in the in-plane and out-of-plane directions, of the bandwidth *W* (top panel), the Ni-O bond length (middle panel) and the <Ni-O-Ni> bond angle (bottom panel). (c) Phase diagram of nickelates summarizing the evolution of T_{MI} and $T_{Néel}$ and how the two transitions are correlated to strain for $NdNiO_3$ and $SmNiO_3$ films compared to the bulk compounds. (b) and (c) after reference [69].

4.1.2 Influence of the substrate orientation

While compressive strain, applied to the most-studied $(001)_{pc}$-oriented $RNiO_3$ films, has been proven to act as an efficient control knob for straightening the Ni-O-Ni angle and thus broadening the system bandwidth, it has been shown that such a control ceases to be effective as the strain verges on the tensile regime, favoring defect formation rather than a continuous evolution of the Ni-O-Ni angle to more distorted values. However, the latter effect can be observed by selecting different crystallographic directions for the growth of $RNiO_3$ films. In particular, the growth of

$(111)_{pc}$ oriented perovskite oxides has received much attention over the past few years, as $(111)_{pc}$-oriented perovskite planes form a buckled honeycomb lattice, which has been predicted to favor the stabilization of exotic electronic phases in TMO-based heterostructures [110,111]. Yet, for several years the study of $(111)_{pc}$-oriented perovskite oxides has been hindered by the difficulties in synthesizing high quality thin films along this crystallographic direction. The strong polarity of $(111)_{pc}$ perovskite planes favors the formation of surface reconstruction or structural and chemical defects that neutralize the polarity in the materials during the growth [112,113]. Nevertheless, intense research efforts have been dedicated to growing $(111)_{pc}$-oriented nickelate films, resulting in high quality defect-free thin samples [93,114-118] which display novel electronic behavior, as discussed in the following.

Interestingly, Lian *et al.*[119] and Catalano *et al.*[93] observe a surprising change of behavior in $NdNiO_3$ films grown under tensile strain on $NdGaO_3$ substrates (ε_{xx}= +1.5%) along crystallographic directions different from the usual $(001)_{pc}$-orientation. Remarkably, the change of orientation dramatically affects the MIT temperature. For example, $NdNiO_3/NdGaO_3$ films oriented along the $(100)_o$ axis ($(110)_{pc}$ in pseudocubic notation) exhibit $T_{MI}\sim200$ K[119], well above the $T_{MI}\sim150$ K displayed by the $(001)_{pc}$ films. Even more strikingly, $(101)_o$-oriented ($(111)_{pc}$ in pseudocubic notation) $NdNiO_3/NdGaO_3$ films display $T_{MI}\sim335$ K and $T_{Néel}\sim200$ K, resembling the $T_{MI} > T_{Néel}$ behavior of more distorted members of the family (see Fig. 9d) [93]. These observations demonstrate that such, less conventional, orientations can stabilize a more distorted Ni-O-Ni angle than in the case of films grown in the $(001)_{pc}$ direction.

Such a profound effect results from a change in epitaxial constraints applied to the system by a given substrate symmetry. In fact, the $NdGaO_3$ substrate is distorted orthorhombically with a B-O-B angle of $\Theta\sim153°$. $NdNiO_3/NdGaO_3$ films oriented in the $(001)_o$ and $(100)_o$ directions have a greater in-plane anisotropy of lattice parameter mismatch at the interface with respect to the $(110)_o$ (corresponding to $(001)_{pc}$) case. This difference in lattice mismatch along the two main in-plane axes imposes a stronger orthorhombic distortion in the film. Lian and coworkers[119] attribute the observed behavior to this effect.

Meanwhile, Catalano and coworkers[93] discuss an alternative epitaxial mechanism occurring at $(111)_{pc}$-oriented film/substrate interfaces. Along the $(001)_{pc}$ direction, each oxygen octahedron is connected to the next through a single apical oxygen, forming a rectangular lattice in the plane, as shown in Fig. 9a. In this configuration, the NiO_6 octahedral units can rather easily adopt the most energetically favorable tilt pattern, balancing the applied strain and the internal chemical pressure [120]. In the case of interfaces normal to the $(111)_{pc}$-direction, on the other hand, each of the corner-

sharing octahedra of the substrate are connected to those of the film through three oxygen atoms instead of only one, imposing a substantially stronger epitaxial requirement. As a consequence, the structure favors a rotation of the NiO_6 units of the film in order to adopt the tilt angle of the substrate, maintaining the connectivity across the interface, as can be visualized in Fig. 9c. In this way the substrate tilt pattern is propagated into the film. Bearing in mind the $R$$NiO_3$ phase diagram [5,97], one can observe on Fig. 9e that the MIT of $(111)_{pc}$ $NdNiO_3$/$NdGaO_3$ at 335 K would correspond to Θ = 153.8°, an angle which is remarkably close to the tilts characterizing $NdGaO_3$ (Θ = 153.2°). Interestingly, the impact of the epitaxial constraints at the $(111)_{pc}$ interface is stunningly robust, affecting up to 17 nm thick $(111)_{pc}$ $NdNiO_3$/ $NdGaO_3$ films.

It is clear, then, that growth along crystallographic directions, different from the conventional $(001)_{pc}$, can be exploited to further implement the control over the MIT in $R$$NiO_3$ films by imposing particular epitaxial constraints to the film lattice. Moreover, these results suggest that selecting such orientations for the deposition of perovskite films could help in engineering novel materials requiring a precise distortion structure. As an example, room-temperature polar metals have been experimentally demonstrated in $NdNiO_3$ and $LaNiO_3$ thin films grown on $(111)_{pc}$-oriented $LaAlO_3$ substrates [116]. The strong constraint imposed by the substrate along the $(111)_{pc}$-growth direction is crucial in achieving the non-centrosymmetric structure in the metallic state. There also exist intriguing theoretical calculations suggesting that exotic topological phases can be stabilized in $(111)_{pc}$-oriented $R$$NiO_3$-based heterostructures [121-123]. Concurrently, Middey *et al.* have recently demonstrated that a novel electronic phase is stabilized in $(111)_{pc}$-oriented $NdNiO_3$ films, as discussed later in this review [117].

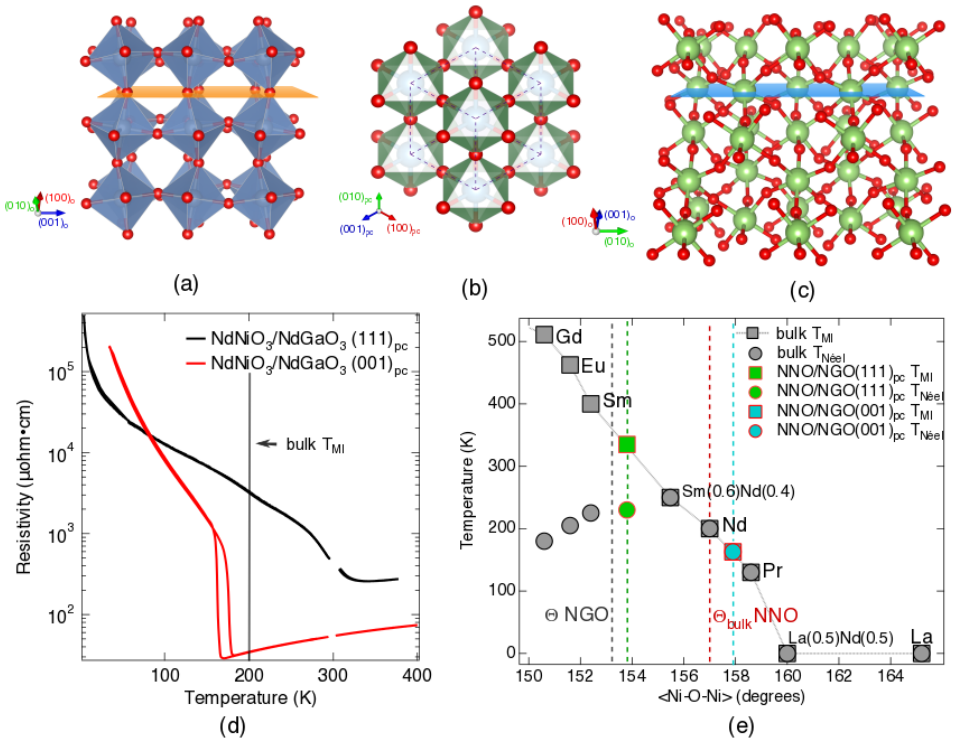

Figure 9: $(001)_{pc}$ and $(111)_{pc}$ interfaces ($(110)_o$ and $(101)_o$ in orthorhombic notation, respectively). (a) Along the $(001)_{pc}$ plane, the connectivity between the BO_6 octahedra is maintained through one apical oxygen only. (b) Top view of the $(111)_{pc}$ plane. (c) Along the $(111)_{pc}$ termination plane, each BO_6 unit shares three oxygen sites with the next one. (d) Temperature-dependence of the resistivity of $NdNiO_3$ films grown on (001) and (111) $NdGaO_3$ substrates. (e) Extrapolation of the Ni-O-Ni angle for $NdNiO_3/NdGaO_3$ based on the experimental T_{MI} and $T_{Néel}$ values of the films and the $RNiO_3$ phase diagram. From Catalano *et al* [93].

4.1.3 Chemical doping effects

Different works have explored the effect of electron (*n*) and hole (*p*) doping on the MIT of nickelates by substitution of the *R* cation. Originally, the first experiments were performed on polycrystalline $NdNiO_3$ samples doped by *R* cation substitution with both electron donor (Th^{4+}, Ce^{4+}) and hole donor (Sr^{2+}, Ca^{2+}) cations [67,124]. Interestingly, it was observed that by varying the dopant concentration between 1% and 10% the MIT is progressively suppressed independent of whether the dopant is *n*- or *p*-type. In particular, García Muñoz *et al.* showed that there are two contributions to the surpression of T_{MI}: (i) the lattice distortion induced by steric effects and (ii) the change in the electron concentration [124]. They observed that while the steric contribution mainly affects the *R*-O distance, the Ni-O bond length is concomitantly modified by the injection of carriers on the Ni site. In fact, the purely electronic contribution plays a major role in controlling T_{MI}, so

that doping with Ce and Th, the size-effect of which is expected to increase the lattice distortion and consequently stabilize the insulating phase, results in a suppression of the MIT due to electron doping. Nikulin *et al.* also studied the consequence of electron doping induced by oxygen non-stoichiometry in polycrystalline $SmNiO_3$ and $NdNiO_3$ [125]. Again, the authors observed a suppression of T_{MI} proportional to the content of oxygen vacancies in the samples, which was varied between 5% and 10%. All together, such studies suggest that light carrier doping induces extra electronic states within the $RNiO_3$ band gap, causing a suppression of T_{MI}.

More recently, the effects of doping have been studied in $RNiO_3$ thin films, providing new important insights on the electronic behavior of these materials. In particular, Ramanathan and coworkers have explored a new approach to electron doping, based on electro-chemical reaction rather than cation substitution [126-128]. In their work, these authors reduced the valence of the Ni cation in $SmNiO_3$ thin films from nominal Ni^{3+} to Ni^{2+} by either oxygen vacancy formation induced by ionic liquid gating or hydrogenation. In both cases, the change of the Ni oxidation state results in a dramatic increase of the room temperature resistivity of the system, which hints at a purely electronically-driven metal-to-insulator transition: meaning that as an extra electron is doped onto the Ni site, the strong Coulomb interaction triggers the electronic localization. While such results may seem to contradict the observations of García-Muñoz *et al.* on bulk compounds, it is important to notice that the doping mechanism investigated by Ramanathan *et al*. is based on a chemical reaction that transforms the Ni oxidation state without modifying the original lattice properties, as in the case of *R*-cation substitution. Interestingly, in a recent work, Heo *et al.* also focused on the effect of oxygen deficiency in $NdNiO_3$ thin films, finding that the insulating phase is stabilized as the oxygen vacancy concentration increases [129], in agreement with the results of Ramanathan *et al*. Concerning the discrepancy with the observations of Nikulin *et al.* on the bulk parent compounds, the authors point out that in previous works the oxygen non-stoichiometry was controlled by varying the oxygen pressure during the growth, a method which affects the oxygen content and the cation stoichiometry concurrently. Conversely, Heo *et al*. controlled the oxygen content of the material by varying the growth temperature of $NdNiO_3$ thin films under tensile strain, succeeding in changing the oxygen stoichiometry independently from the *R*-cation stoichiometry.

4.1.4 Electric Field Effect

In addition to strain engineering and optical excitation, the transport properties of RNiO$_3$ films have also been investigated by field effect (FE) experiments, allowing the charge carrier density of the RNiO$_3$ conducting channel to be modulated as a function of gate voltage applied through a dielectric or ionic liquid layer. FE-based devices have been realized with LaNiO$_3$ [130], NdNiO$_3$ [53,131] and SmNiO$_3$ films [126,132]. In LaNiO$_3$ /SrTiO$_3$ heterostructures, a 10% change of the carrier density of a 6 u.c. thick LaNiO$_3$ conducting channel was obtained by applying a gate voltage varying from 300 to -300 V through the SrTiO$_3$ dielectric layer, indicating that *p*-type conduction dominates the transport characteristics of the device [130]. Analogous measurements performed on NdNiO$_3$/LaAlO$_3$ films demonstrated FE as a practical tool for tuning the temperature of the MIT over a 50 K range[53]. These measurements took advantage of the electric double layer transistor (EDLT) FE technique, in which an ionic liquid allows an in-plane 2D carrier density modulation of the order of 10^{14} - 10^{15} cm^{-2} to be achieved. We will see in a later section that such a tuning of electronic properties opens the way for nickelate-based transistors. Motivated by these promising results, Son *et al.* propose the design of RNiO$_3$-based modulation-doped Mott FE transistor (MMFET), in which an MIT can be switch on and off through the applied gate voltage [131]. Marshall *et al.* have realized a ferroelectric field effect device which exploits the resistivity modulation of an LaNiO$_3$ conducting channel induced through a ferroelectric Pb(Zr,Ti)O$_3$ gate [133]. Similar ferroelectric field effect devices have also been designed adopting Sm$_{0.5}$Nd$_{0.5}$NiO$_3$ films as conducting channel [134,135]. Finally, Shi *et al.* have developed an original SmNiO$_3$-based FE transistor, which mimics the behavior of neural synapses [127], whose concept and operation are described extensively in section 6.2.1.

4.1.5 Pump-probe experiments

An interesting series of pump-probe experiments carried out by the group of Cavalleri demonstrates dynamic light control of the RNiO$_3$ electronic phases. Caviglia *et al.* [136] succeeded in melting the charge-ordered insulating phase of NdNiO$_3$ thin films by pumping the system with light pulses tuned to photon energies between 70 and 130 meV. As the sample is cooled down to $T < T_{MI}$, the light excitation induces a long-lived (> 1 ns) metastable metallic phase, revealed by transient change of the reflectivity probed in the near- and far-infrared (IR) range. Intriguingly, such an effect is supported by selective optical excitation of an IR-active phonon mode in the substrate (LaAlO$_3$ or NdGaO$_3$), which triggers the melting of the insulating phase. An analogous behavior was observed

for $SmNiO_3/LaAlO_3$ films [137], whose response could be probed over a remarkably broad THz range (100-800 cm^{-1}). In addition, by pumping the system in both $T_{Néel} < T < T_{MI}$ and $T < T_{Néel} < T_{MI}$ temperature ranges, the authors also demonstrate that the charge order melts regardless of the presence of the antiferromagnetic ordering.

In order to clarify the underlying physics of such dynamically excited metastable metallic phases, Caviglia *et al.* and Först *et al.* carried out a series of measurements combining optical excitation with time-resolved non-resonant and resonant x-ray diffraction [138-140]. By identifying and following the diffraction peaks characterizing the charge-ordered ($(½\ ½\ ½)_{pc}$) and antiferromagnetically-ordered ($(¼\ ¼\ ¼)_{pc}$) superstructures of the $RNiO_3$ insulating phase, the authors could directly investigate the time-dependent evolution of the melting and disentangle the dynamics of the charge, spin and lattice degrees of freedom across the insulator to metal transition (IMT). Most notably, they found that the melting of the insulating phase begins at the buried film/substrate interface and propagates through the film faster than the bulk speed of sound of the material, indicating an electronic mechanism driving the IMT. In particular, further analysis reveals that ultrafast charge redistribution is at first induced after dynamic light excitation and is followed by the melting of the spin ordering, while both the charge and spin redistributions evolve faster than the phonon speed in the films.

4.2 The case of $LaNiO_3$ thin films

Within the family of rare earth nickelates, $LaNiO_3$ is the odd-one-out as it remains paramagnetic and metallic at all temperatures in bulk[A]. When grown in the form of ultrathin layers, however, $LaNiO_3$, in common with the other $RNiO_3$s, enters an electronically localized state with no observed bond disproportionation [71,141]. As dimensionality is reduced, the films first go from a metallic regime to one where a resistivity upturn is seen, which has been attributed to weak localization. The critical thickness whereupon the films become insulating can vary from 2 – 6 u.c., depending on the substrate selected for epitaxial growth [52,130,141]. This thickness-dependent transport behavior is likely driven by a profound alteration to the electronic structure of $LaNiO_3$, marked by drastic changes to the Fermi surface upon reducing the thickness towards the atomic limit, as photoemission studies have shown (Fig. 10a) [48 142].

[A] The recent results reported in Ref. [38] Z. Li, H. Guo, Z. Hu, L. Zhao, C.-Y. Kuo, W. Schmidt, A. Piovano, T. Pi, D. Khomskii, and L. Tjeng, arXiv preprint arXiv:1705.02589 (2017).) indicate an antiferromagnetically ordered state for very low resistivity single crystals.

This behavior may have a largely structural origin. Hardening of the phonon modes associated with oxygen octahedral distortions, concomitant with the dimensionality-induced electronic localization, has recently been reported [143]. In the same study it was found that the film structure differentiates into three different local structures – one found on the surface, one towards the interface with the substrate and the third in the interior layers where the boundary effects are minimal. See Fig. 10c. Indeed, it has been shown that the polar $LaNiO_3$ surface is prone to developing buckling distortions, as illustrated in Fig. 10b, which very likely leads to an increase in the resistivity through a reduction of the orbital overlap [144]. This effect can be mostly alleviated with the addition of an encapsulating layer of, for instance, $LaAlO_3$ but when it comes to ultrathin films, 1-2 u.c., not even this is enough to preserve the metallic state.

Efforts to understand the nature of the ultrathin insulating state of $LaNiO_3$ are ongoing. Oxygen vacancies, interfacial cation intermixing, dimensionality, electron-phonon coupling or defects could all have a part to play.

Another possibility is that $LaNiO_3$ undergoes multiple structural phase transitions under strain, with different structures under compression and tension [145,146]. Beyond the experimentally observed phase transitions, it is important to note that calculations suggest additional structural instabilities, hinting at a rich energy landscape, which are expected to impact electronic properties.

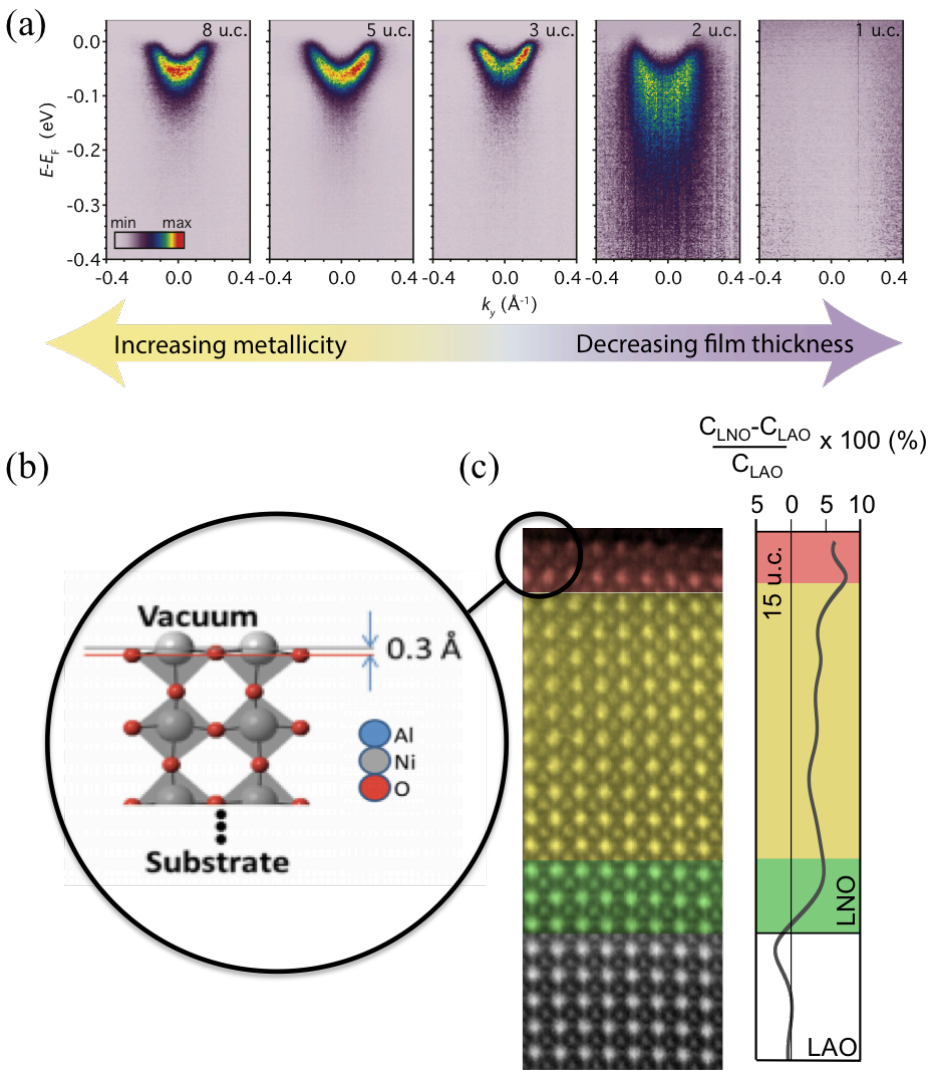

Figure 10: (a) A photoemission study showing the disintegration of the Fermi surface as the thickness of $LaNiO_3$ is decreased to only 1 u.c. [48] (b) Surface buckling of Ni-O-Ni bonds [144] and (c) local structure differentiation as revealed by transmission electron microscopy[143].

There remains a strong focus on $LaNiO_3$ as a potential building block in oxide-based functional materials, driven, in large part, by the prediction of possible high-temperature superconductivity in $LaNiO_3$-based heterostructures. A key ingredient in achieving this is a large Ni orbital polarization, further discussed later [147]. There are clearly limitations to the orbital polarizability of thin films of $LaNiO_3$. One issue, which is general to perovskites, is the aforementioned tendency for the NiO_6 octahedra to rotate, rather than to adopt a Jahn-Teller distortion, under the influence of biaxial strain [148]. The octahedra are able to remain rigid under a rotational distortion and thus the immediate oxygen coordination environment would retain an almost cubic symmetry. Also, there is predicted

to be a strong on-site Hund's rule coupling [149], which would directly oppose the high degree of preferential occupation that is sought after.

One possible avenue to explore with thin layers of $LaNiO_3$ is to go one step further and include them in a multilayer heterostructure. The study of multilayers containing $LaNiO_3$ will be discussed in the following section.

5. THIN FILM MULTILAYERS

5.0 Motivation

Modern advances in synthesis techniques allow the fabrication of digital oxide multilayer heterostructures, or superlattices, of very high quality, comparable to that of semiconductors. In this context, superlattices have become a very powerful route toward manipulating the electronic states of TMOs by exploiting interface-driven phenomena and reduced dimensionalities. Nickelates are no exception and nickelate-based superlattices open up a variety of avenues to further control their functionalities and realize novel collective phases.

5.1 $LaNiO_3$-based multilayers

In addition to the interest in nickelate thin films as the closest system to single crystals and the capabilities they offer to tune their electronic transitions, it is fair to say that the present wave of interest in nickelates has been motivated by the previously mentioned prediction of Chaloupka and Khaliullin. They propose that a novel high temperature superconductor may be designed by orbital engineering in 1-unit-cell-thick $LaNiO_3$ layers sandwiched between layers of an isostructural insulating oxide $LaXO_3$ (X = Al, Ga, Sc, etc.) [147]. One of the core requisites for the successful fabrication of a synthetic superconductor is a high degree of Ni orbital polarization. The most intuitive way to achieve this is to break the symmetry of the Ni environment, which happens naturally when going from a bulk material to a thin film. Ideally, a stretching (or squashing) of the NiO_6 octahedra would be induced by the application of biaxial compressive (tensile) strain and result in a preferential occupation of the $3z^2 - r^2$ (x^2 - y^2) orbitals. The *ab initio* calculations predicting the formation of a cuprate-like Fermi surface in these heterostructures were further supported by DFT+DMFT studies including an accurate treatment of electronic correlations [150,151].

Experimentally, orbital polarizations of up to 25% have been achieved in two-component (4u.c. $LaNiO_3$/ 4u.c. $GdScO_3$) superlattices grown under compressive strain (see Fig. 11a) [152]. The development of a new methodology based on x-ray absorption and resonant reflectivity

measurements has allowed the orbital occupation profile, and thus the orbital polarization of the interface and inner layers, to be quantified [153]. These studies have revealed that the strain induced by lattice mismatch provides the largest effect compared to the chemical composition of the blocking layers. In $LaNiO_3/LaAlO_3$ superlattices, an asymmetry in strain-dependent orbital occupation has been reported, with tensile strain acting on orbital polarization and compressive strain on octahedral distortions [154]. A more recent alternative route proposes enhancing orbital polarization in $LaNiO_3$-based heterostructures through engineering of atomic-scale structural distortions in tri-component superlattices [155]. Doping the nickelate layer via interfacial charge transfer and breaking inversion symmetry through the introduction of a third chemical compound in the heterostructures has led to orbital polarizations of up to 50% in atomically layered superlattices of the type (1 u.c. $LaTiO_3$/1 u.c. $LaNiO_3$/1 u.c. $LaAlO_3$), as illustrated in Fig. 11b [156]. The attained orbital polarization values and the difficulty in achieving a single band crossing the Fermi level in $LaNiO_3$-based superlattices are explained by DMFT calculations including the oxygen bands and the important role of correlations through the Hund's rule coupling [149,157].

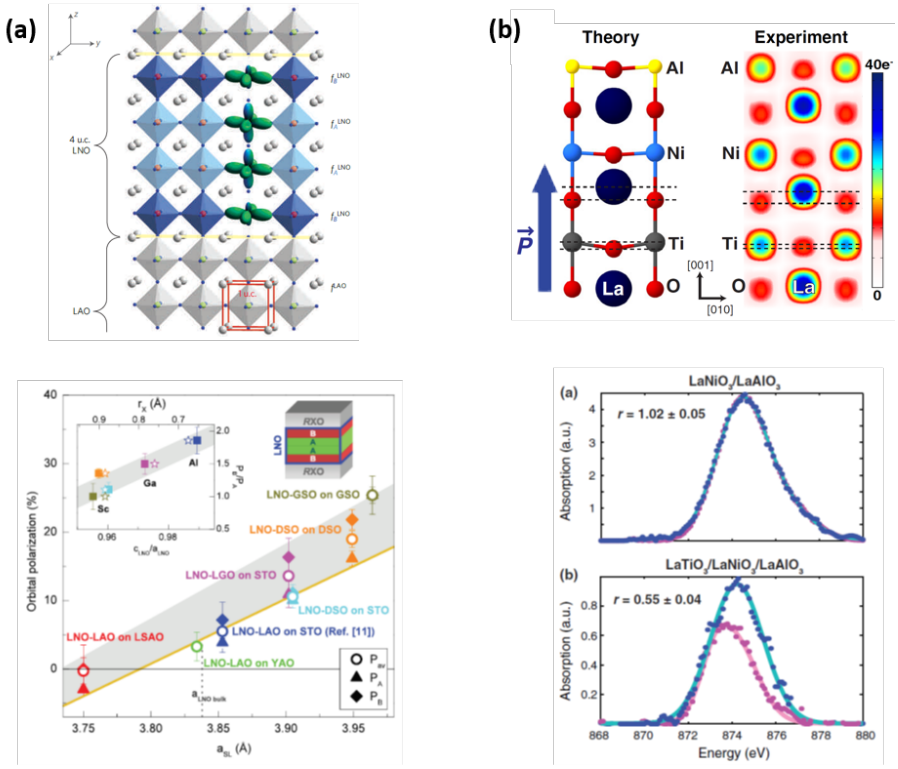

Figure 11: Engineering orbital polarization in $LaNiO_3$-based superlattices. (a) Schematics of the evolution of the Ni 3d e_g orbital occupation in $LaNiO_3$-$LaAlO_3$ superlattices, and orbital polarization values inferred from x-ray absorption spectroscopy (XAS) and reflectivity measurements for several $LaNiO_3/LaXO_3$ (X = Al, Ga, Sc) superlattices grown on a variety of substrates. Adapted from references[152,153]. (b) Theoretically and experimentally determined atomic

structures for (1u.c. $LaTiO_3$/1u.c. $LaNiO_3$/3u.c. $LaTiO_3$) showing the polar displacements, and XAS spectra acquired with linearly-polarized light for two- and tri- component nickelate superlattices where *r* is the hole ratio quantity related to orbital polarization. Adapted from references [155,156].

In general, the transport properties of $LaNiO_3$-based superlattices reflect the thickness-driven metal-insulator transition observed in the corresponding nickelate thin films [48,52,130,158]. For example, an evolution from a variable range hopping transport regime to a gapped insulator is observed in $SmMnO_3$/$LaNiO_3$ multilayers as the $LaNiO_3$ thickness is reduced below 4 unit cells [159]. $LaNiO_3$-based heterostructures have also proved to be model systems for engineering octahedral rotations [159,160]. Although the localized state of those heterostructures involving ultrathin $LaNiO_3$ layers is another limiting factor in the efforts towards superconductivity engineering [156,161], this insulating state has allowed the emergence of other exciting collective phenomena such as the development of an antiferromagnetic phase in $LaNiO_3$ with a $(¼\ ¼\ ¼)_{pc}$-propagation vector, like all the other nickelates in the insulating phase. This emergent magnetic structure was first shown in $LaNiO_3$/$LaAlO_3$ superlattices [161], and later reported in other $LaNiO_3$-based heterostructure multilayers [71,118]. Magnetic ordering develops only as the $LaNiO_3$ blocks in the superlattices are reduced below a critical thickness (which depends on the film orientation and strain) but it should be noted that no evidence of the charge-disproportionation present in the other insulating nickelates has been reported so far [162]. Moreover, as shown in Fig. 12a, the polarization plane of this spiral magnetic state configuration can be modified by controlling the Ni d-orbital occupation through strain and spatial confinement [71]. Very recently Lu *et al.* have performed RPA calculations showing that, as the thickness of $RNiO_3$ films is restricted to less than 3 u.c., the charge instability is suppressed, whereas the spin instability at $q_{Bragg} = (¼\ ¼\ ¼)_{pc}$ becomes predominant and drives the emergence of a spin density wave, providing a solid theoretical framework for the experimental results mentioned above.

Thus, despite the lack of the observation of the superconducting phase predicted by Chaloupka and Khaliullin, the investigation of their proposal has provided a catalyst for remarkable discoveries concerning dimensional and interfacial effects on the electronic structure of $LaNiO_3$, demonstrating the possibility of broadening the phase diagram of the material to a novel extent.

$LaNiO_3$-based superlattices have also been widely investigated in combination with manganites, where interfacial charge transfer between Ni and Mn is at the origin of many interesting phenomena [115,163-166]. In $LaNiO_3$/$LaMnO_3$, charge transfer occurs from Mn to Ni due to the difference in electronegativity with the resulting (nominal valence) Ni^{2+}-Mn^{4+} cations interacting strongly ferromagnetically [165,167-169]. Exchange bias has been observed at low temperature in

$LaNiO_3/LaMnO_3$ superlattices [115,168], with various models having been proposed to explain this unexpected behavior [118,170,171]. Interestingly, when grown along the less conventional $(111)_{pc}$ direction and for digital superlattices of 7-monolayer-thick-$LaNiO_3$, exchange bias has been observed at low temperature followed by an antiferromagnetically-coupled state between the $LaMnO_3$ layers [118]. This complex magnetic evolution is the result of a subtle interplay between interface-driven phenomena and reduced dimensionality leading to the stabilization of a $(¼\ ¼\ ¼)_{pc}$ magnetic spiral structure in $LaNiO_3$ (see Fig. 12c).

For $LaNiO_3/La_{2/3}Sr_{1/3}MnO_3$ superlattices, an oscillatory interlayer coupling between the manganite layers depending on the thickness of the $LaNiO_3$ spacers occurs [164 172]. As depicted in Fig. 12c, such a non-collinear coupling has recently been explained by the formation of a helical spin structure within the $LaNiO_3$ layers, which persists almost up to room temperature [173].

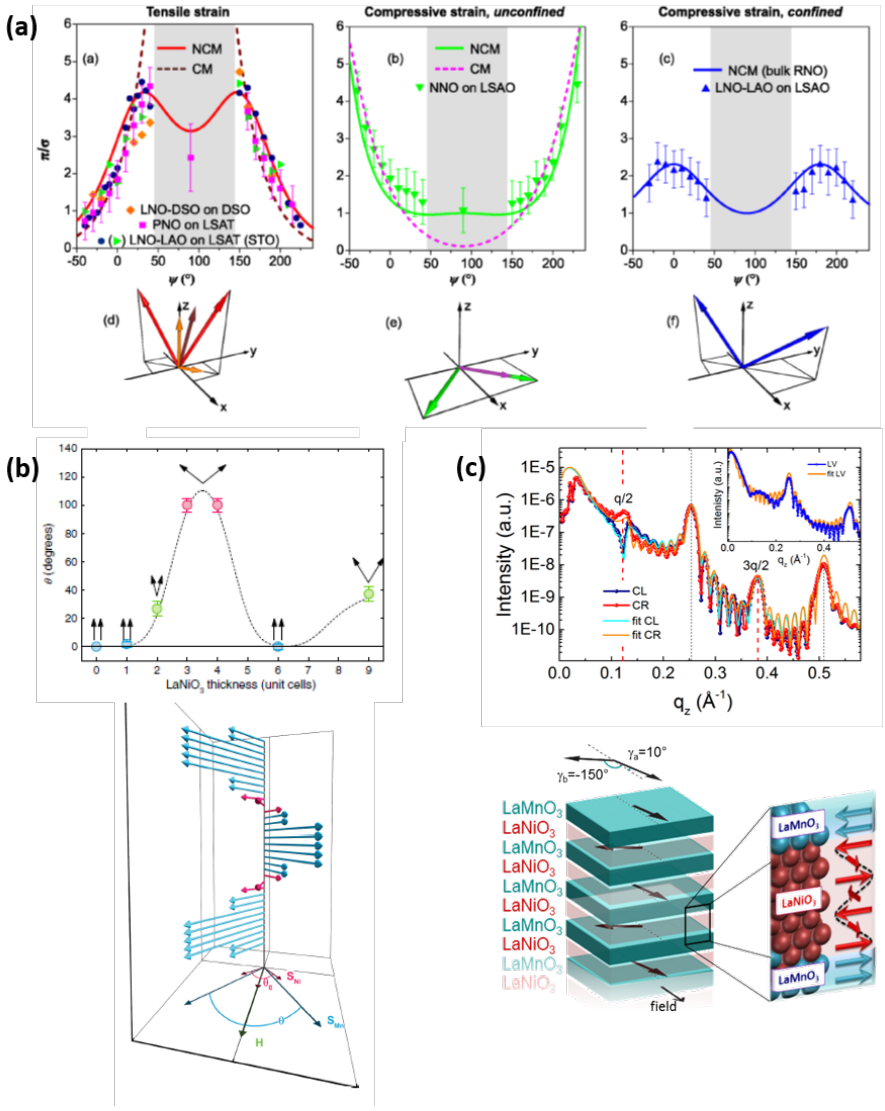

Figure 12: Magnetism in $LaNiO_3$-based superlattices. (a) Polarization-dependent azimuthal scans used to infer the polarization plane (illustrated by the arrows) of the nickelate antiferromagnetic spiral structure under tensile and compressive strain for (2u.c.$LaNiO_3$/2u.c.$LaAlO_3$) and (2u.c.$LaNiO_3$/2u.c.$DyScO_3$) superlattices and nickelate ($PrNiO_3$, $NdNiO_3$) thin films. The same color code is used in the measurements and sketches of the spin directions. Adapted from [71]. (b) $LaNiO_3$-thickness-dependent non-collinear oscillatory coupling in $(LaNiO_3)_N/(La_{2/3}Sr_{1/3}MnO_3)_9$ superlattices and a schematic of the magnetic structure for the superlattice with 3 u.c. $LaNiO_3$ layers, where the manganite and nickelate layers are shown in blue and pink, respectively. Adapted from[173]. (c) The observation of half-order peaks in polarized reflectivity measurements at the Mn L_3-edge of $(111)_{pc}$-oriented 7-monolayer-thick $LaNiO_3/LaMnO_3$ superlattices reveals an antiferromagnetically-coupled state between the manganite layers triggered by the digital nature of the nickelate layer. Adapted from[118].

In superlattices of $LaNiO_3$ and the insulating paramagnet $CaMnO_3$, interfacial ferromagnetism confined to 1 unit cell in the manganite layer has been reported only for periodicities involving metallic $LaNiO_3$ layers ≥ 4u.c. and attributed to double exchange resulting from charge transfer (in this case from Ni to Mn, given the initial Mn^{4+} state in $CaMnO_3$)[166] .

Rich behavior is also observed in superlattices combining members of the nickelate and titanate families. In particular, charge transfer is expected to occur from the titanate to the nickelate layers due to the difference in the electron affinities of the two materials [174]. Interestingly, the resulting electronic reconstruction has been proposed to enhance electronic correlations in superlattices of $LaNiO_3$ and the Mott insulator $LaTiO_3$ [175]. Experimentally, a correlated gap of 1.5 eV has been estimated for the insulating (2 u.c. $LaNiO_3$/2 u.c. $LaTiO_3$) superlattices, which also exhibit enhanced orbital polarization ($n_{dx2-y2} > n_{3z2-r2}$) and a splitting of the Ni e_g band attributed to interfacial structural distortions [176].

5.2 *R*NiO_3-based multilayers

Besides $LaNiO_3$, other members of the *R*NiO_3 family have been integrated into various heterostructure multilayer designs, exploring an ensemble of interfacial effects induced at the interface between the nickelates and other perovskite compounds.

Grisolia *et al.* have studied the charge transfer at the titanate/nickelate interface in a series of bilayers consisting of 7 u.c. of *R*NiO_3 (*R* = La, Nd, Sm) deposited on 7 u.c. of $GdTiO_3$ on top of a $LaAlO_3$ single crystal substrate [174]. Spectroscopy measurements confirm charge transfer from the titanate to the nickelate layers, the number of transferred electrons being controlled by the choice of the rare earth cation in the *R*NiO_3 layer.

Inspired by the $LaNiO_3$-based superlattice design proposed by Chaloupka and Khallioulin, a number of works have focused on heterostructures wherein $RNiO_3$ layers alternate with some insulating perovskite acting as a charge spacer (typically, a member of the $RAlO_3$ family). Hepting *et al.* have shown that the charge ordered phase of bulk $PrNiO_3$ can be suppressed in ($m PrNiO_3/n PrAlO_3$) superlattices, as they observed a magnetically ordered ground state in the absence of the bond length disproportionation [105]. Promising results have also been attained with the study of $(mNdNiO_3/nLaAlO_3)_N/LaAlO_3$ superlattices grown along the $(111)_{pc}$ crystallographic direction [117]. The $NdNiO_3$ film embedded in such a system is found to host an orbitally-ordered ground state and to display sizeable antiferromagnetic correlations absent in the bulk counterpart or in the $(001)_{pc}$-oriented analogous superlattices. In particular, the stabilization of this unique electronic phase is ascribed to the confinement of the Ni *3d* electrons onto the hexagonal lattice enforced by the $(111)_{pc}$-oriented perovskite surfaces.

Finally, Girardot *et al.* investigated the properties of the first all-nickelate multilayers, alternating $SmNiO_3$ and $NdNiO_3$ thin films [177]. In their work, the authors compare the complex evolution of the Raman spectra of epitaxial films of the mixed compound $Sm_{0.6}Nd_{0.4}NiO_3$ and of $(nSmNiO_3/nNdNiO_3)_N$ superlattices, with the periodic thickness, *n,* varying from 100 u.c. down to 25 u.c. The resistivity vs. temperature curve of an $((SmNiO_3)_{100}/(NdNiO_3)_{100})_1$ bilayer shows two transitions: (*i*) a first hysteretic transition upon heating at $T_{MI} \approx 160$ K, which is very close to the value of $T_{MI} = 158$ K for bulk $NdNiO_3$. (*ii*) a second transition, less pronounced at $T_{MI(2)} \approx 370$ K, which shows no hysteresis, similar to $SmNiO_3$; this temperature is lower than $T_{MI} = 393$ K of a single bulk-like $SmNiO_3$ film, an effect likely due to strain.

6. SCOPE OF APPLICATIONS

6.0 Context

The early years of study on nickelates were naturally focused on the understanding of their fundamental behavior, namely the MI phase transition, the magnetic structure and the connection between the two, as discussed earlier. In addition to this ongoing quest, many of the more recent studies are marked by the exploration of potential application of nickelates in a variety of devices. This interest in applications has been triggered by several developments.

Correlated TMOs, in general, have attracted increasing attention due to their remarkable variety of functionalities, linked to their fascinating electronic, magnetic and optical properties. This raises the potential for new types of electronic devices. A distinctive element of complex TMOs is the

competition of electronic phases close to a phase boundary [178], which is often highly sensitive to subtle structural changes [8]. One of the properties observed in some correlated TMOs, absent in conventional semiconductors, is the sharp metal-insulator phase transition, as discussed previously, which can be tuned by external stimuli. Already this functionality can be exploited in a variety of applications (see e.g. Refs. [126,131,179-182]), thus offering great potential to make use of the MIT in nickelates.

In addition to MBE, PLD and sputtering, as discussed previously, more large-scale growth of perovskite compounds is also feasible. This possibility, often coupled with nanofabrication, means that realization of actual devices can go alongside the increasing range of device concepts inspired by the more fundamental study of nickelates reviewed so far.

Table 1 summarizes the main device concepts reported so far, without claim for full completeness. While most of the propositions today concern single layers, this application landscape is extended by the additional opportunities arising from perovskite multilayers integrating, or entirely consisting of, nickelates.

Table 1

Overview of applications proposed in literature for rare earth nickelates, *R*NiO_3

Application field	Application	Investigated material	References
Electrode material	Anode	$LaNiO_{3-\delta}$	183
	Supercapacitor	$LaNiO_3$/NiO	184-188
	In heterostructures	$LaNiO_3$	189-198
	Buffer layer in HTS	$LaNiO_3$	199-202
Opto-electronics	Tunable Photonics	$SmNiO_3$	127,203,204
	Photodetection	$GdNiO_3$	205
	Thermochromism	$SmNiO_3$, $NdNiO_3$	206-208
	Photovoltaics	$NdNiO_3$	209,210
Ion-conduction/ catalysis	Fuel Cell, SOFC	$SmNiO_3$	211,212
	Oxygen reduction	$LaNiO_3$	213-216
Resistance Switching	Neuromorphic device	$SmNiO_3$, $NdNiO_3$	126,217-219
	Neuromimetic circuits	$SmNiO_3$	220
	Synaptic transistor	$SmNiO_3$	126
	Transistor	$LaNiO_3$/Si	221
	Mott Transistor	$NdNiO_3$	131,222

	Proton-gated transistor	$SmNiO_3$	127
Sensing	Gas sensing	$LaNiO_3$	186,223-233
Magnetism	Magnetotransport Multiferrocity	$SmNiO_3$ $SmNiO_3$, $NdNiO_3$	234 235-237

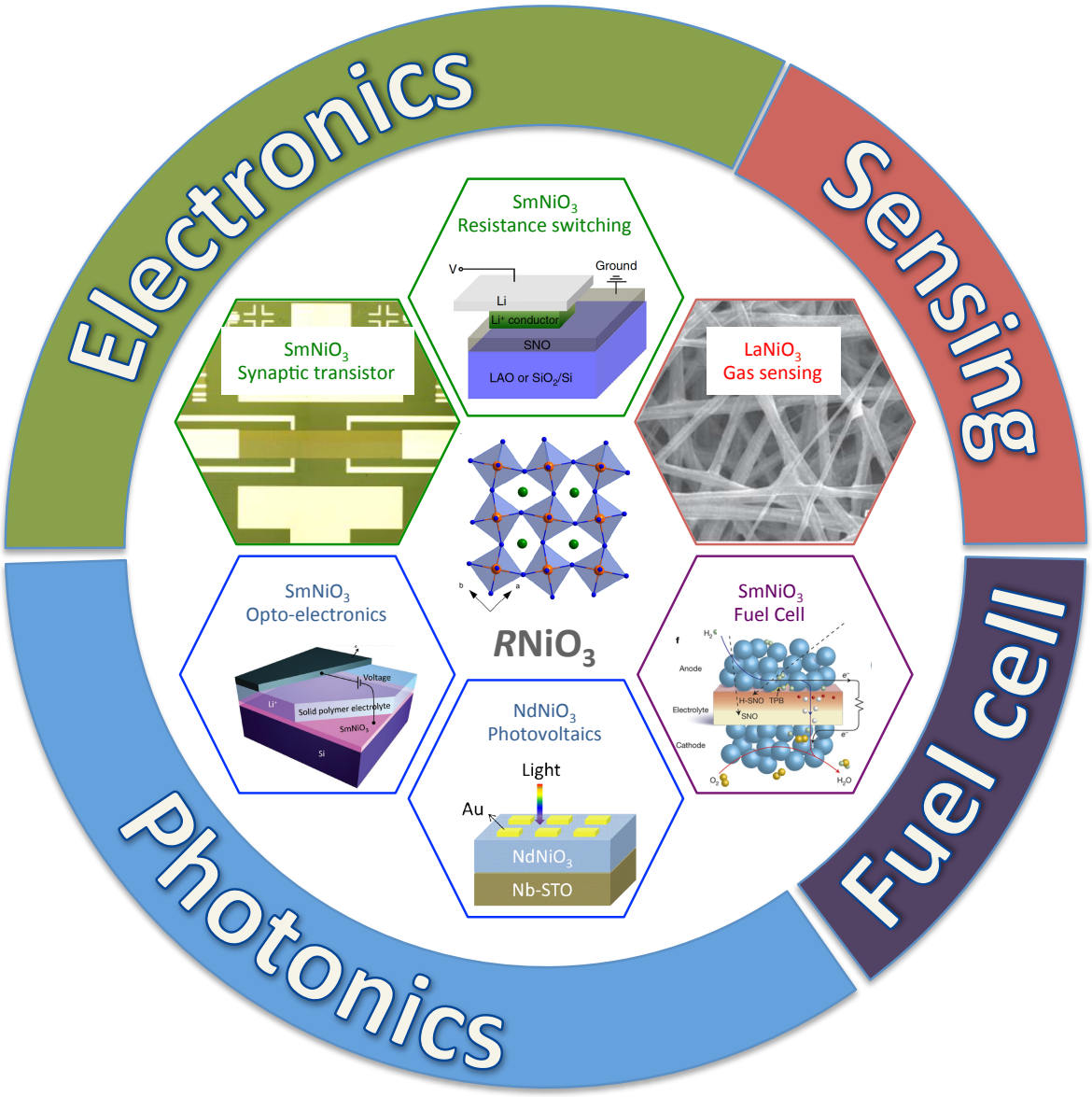

Figure 13: Schematic view of potential applications of RNiO$_3$ in the field of electronics, photonics, sensing or fuel cells. The images inside the hexagons are adapted from literature and address specific application examples such as photovoltaics[209], opto-electronics[203], sensing[186], fuel cells[128], resistance switching[127] and synaptic transistors[238]. For a more complete list of applications, please refer to Table 1.

6.1 Exploiting the conductivity of $LaNiO_3$

In number, the most discussed nickelate in view of applications is $LaNiO_3$. $LaNiO_3$ is the only perovskite nickelate that is metallic at all temperatures in bulk. Its low electrical resistivity of about 100 μΩ·cm, makes it a good candidate for the electrode material in oxide-based microelectronic devices. In most of the reported application schemes, $LaNiO_3$ is implemented in oxide heterostructures as a metallic layer and electrode, rather than as a functional element. The literature on such structures is vast and we cite only some representative references [189-198]. As a matter of fact, together with the perovskite $SrRuO_3$, $LaNiO_3$ stands out as the preferred candidate perovskite for a top or bottom electrode of all-perovskite microelectronic devices. When comparing $LaNiO_3$ and $SrRuO_3$, we note that $SrRuO_3$ has been reported to have the tendency to develop a rougher surface at either small (< 30 nm) or large thickness (> 100 nm)[239]. In such cases, a highly defective and possibly low dielectric interface may form between the electrode and the active layer, predictably resulting in degraded functional performance. $LaNiO_3$ seems less affected by these limitations with the exception of the formation of cracks at very large thickness (> 300 nm), and therefore appears to be a versatile electrode material. However, the conductive properties of $LaNiO_3$ can be altered in ultrathin epitaxial films, as previously discussed [240,241]. Finally, we note that $LaNiO_3$ has the added advantage that it is inexpensive compared to other oxides such as $SrRuO_3$. Having said all this, the integration of $LaNiO_3$ in all-perovskite devices relies on the scalability of high quality $LaNiO_3$ thin films.

In a few applications the conductivity of $LaNiO_3$ is more directly exploited as a functional/active part of a device. Examples include its use in oxygen reduction in the field of catalysis [213-216], in water electrolysis [183], in fuel cells, in gas sensing [186,223-233] or super-capacitors [184-188]. Finally, for completeness, we note that $LaNiO_3$ is also considered as a conductive oxide buffer layer on textured Ni tapes for high-T_c-coated superconductors (HTS) [199-202], providing both an epitaxial template for

the HTS layer and electrically coupling the HTS layer to the metallic tape substrate, for instance in the so-called RABiTS technology.

6.2 Exploiting the Metal-to-Insulator transition and associated properties

While applications of $LaNiO_3$ rely on the fact that its conductivity remains high and rather stable over a large temperature-range, the other members of the rare earth nickelates attract interest for their abrupt and sharp MIT and its related properties, such as resistive switching or changes in optical and opto-electronic properties. Most literature reports concern either $SmNiO_3$ or $NdNiO_3$, with considerable focus on the former, which has an MIT above room temperature (130 °C) allowing its potential integration into oxide electronics based on CMOS technology [217]. The fine control of the MI transition temperatures in nickelate thin films by multiple parameters is critical for developing their potential in various applications.

MITs in TMOs are a longstanding topic in materials physics and chemistry, and the variety of possible mechanisms triggering them in different materials has been discussed in a number of reviews, in addition to the present one, see e.g. Ref. [59]. The exploration of MI transitions in applications has also been much discussed in literature and many of the currently suggested device concepts for nickelates have been inspired by ideas proposed for other TMOs such as VO_2 and related oxides [182]. Within this review, we will mainly focus on the advances that have been explored more recently and that reveal a high potential for new innovative devices, based, for instance, on resistance switching or opto-electronic properties.

6.2.1 Resistance Switching

One of the most popular applications discussed in recent literature on nickelates relates to their memristive behavior, which is closely related to the MIT. Beyond nickelates, nano-scale resistive switching devices, sometimes termed memristors, have recently generated significant interest for their use in memory, logic and neuromorphic applications [242].

The term resistance switching is used here to describe the memristive behavior observed in some nickelate devices. It should not be confused with the resistive switching behavior observed in many oxides (see for instance Ref. [243]) and related to the formation of filamentary conducting channels linked to oxygen vacancy formation. Generally speaking, memristors stand in the context of an increasing exploration, by the electronic engineering community, of novel paradigms for

information processing inspired by the operation of the brain, i.e. neuromorphic computation schemes. In a simplified vision, the brain is based on two types of building blocks: synapses and neurons. Neurons integrate the information received from other neurons and emit a spike of voltage when the integrated level reaches a threshold. Synapses connect two neurons and modulate the ease with which information is transmitted; the tunability of their "transmissivity" or synaptic weight is at the heart of the learning process. Building a neuromorphic computation architecture thus requires building electronic equivalents of the synapses and of the neurons [220]. While neurons can be emulated by just one CMOS transistor, synaptic behavior is harder to mimic with classical circuits. This has motivated the development of a new hardware component able to replicate the behavior of synapses: the memristor.

Memristors are simple two-terminal analogue nanodevices whose resistance varies with the voltage (or current) they previously experienced. A memristor is also known as the fourth fundamental circuit element, in addition to the better known resistor, capacitor and inductor [244]. Memristors act as "resistors" with "memory", hence the name [245]. The analogue response of memristors, the adjustability of their resistance level and their non-volatile character qualifies them as electronic synapses. The overall interest of memristors was renewed in 2008 by the discovery of $Pt/TiO_2/Pt$ memristors, in which coupled migration of electrons and ions within the TiO_2 layer results in a continuous change of the total device resistance [246]. This voltage-induced displacement of ions at the nanoscale may hinder reliability and endurance. Another proposed alternative is a ferroelectric memristor[247,248], namely a tunnel junction based on a ferroelectric barrier, whose tunnel resistance varies greatly depending upon the polarization direction of the barrier (pointing towards one or the other electrode) and on the associated ferroelectric domain structure. Such ferroelectric memristors are purely electronic and based on the control of ferroelectric domain structures. Among the competing memristor concepts we may also cite anionic electronic conducting oxides [249,250].

Within this attractive field where different concepts and material classes compete, oxides with an MIT have been proposed as alternative candidates [245,251]. The first experimental demonstration of an MI-based memristor was described by Driscoll *et al.* [245] for VO_2 thin films. Importantly, the authors view their observations from the perspective of "phase-transition-driven memristive systems", where the hysteresis with its local characteristics gives the memory aspect of the memristor. Inspired by this, Ramanathan and co-workers[217] have proposed exploiting the MIT in $SmNiO_3$, for which they report memristive characteristics that are the basis for their subsequent work on synaptic transistors [126] or neuromimetic circuits [220]. In a first step, these authors synthesized $SmNiO_3$ thin films on $LaAlO_3$ and Si substrates to realize systems with charge transport characteristics for both

in-plane and in out-of-plane devices[217]. For the $SmNiO_3/LaAlO_3$ structures, they report results that suggest a history-dependent memristive behavior, opening the door to device applications based on this resistive switching. In a later work, they propose a $SmNiO_3$-based transistor that mimics a biological synapse, by doping the $SmNiO_3$ through an ionic liquid [126]. Finally, the observation of a colossal resistance switching by electron doping may be one of the avenues toward larger conductance changes, opening up a greater scope for future applications [127].

The work on $SmNiO_3$ has motivated similar studies on $NdNiO_3$ heterostructures with the originality of including an asymmetric proton concentration [218]. Altogether, the demonstration of memristive behavior in nickelates broadens the landscape of materials conceivable for future memristive applications with the potential to parallel biological neural systems with circuit architecture [220]. Nickelates are competitive in this respect due to the large panel of parameters that can modulate their electric response. A remaining question is how the presence of a structural phase transition affects the cyclability.

Finally, as discussed in section 4.1.3, we stress that extrinsic effects such as doping or oxygen vacancies (natural or induced by an electric-field) are expected to strongly influence the Mott phase transition by a drastic change of the Ni carriers. This, in turn, offers additional complexity and tuning parameters for memristors (or other applications).

6.2.2 Opto-electronic properties

An MI phase transition is naturally accompanied by dramatic changes in optical properties. Tuning the MIT is thus intimately linked to the tuning of opto-electronic properties, which are the basis for a large number of photonic applications ranging from smart glasses and photovoltaics, to the coatings with tunable emissivities, to optical memories or photosensors and many others. Generally speaking, one of the main challenges is to integrate nickelates into optical devices, a task which requires skilled nanofabrication and adapted device architectures. Within the field of opto-electronics, band-gap engineering of TMOs is among the most active and challenging fields and opens a number of applications.

Among different parameters, opto-electric properties of perovskite nickelates are sensitive to their oxygen content, which allows their electronic structures to be adjusted by varying the oxygen partial pressure during film deposition. It has been shown[205] that this route can be exploited to engineer the properties of $GdNiO_3$ films so that they are sensitive to a broad range of wavelengths. By combining the $GdNiO_3$ film with Nb-doped $SrTiO_3$ in a heterojunction, the authors of Ref. [205]

have designed a self-powered photodetector with high sensitivity to light with a wavelength between 365 nm and 650 nm. It is reported that the performance remains remarkably stable even after 6 months [205].A similar band gap tuning has been reported for $NdNiO_3$, leading to the claim of potential for novel photovoltaic devices [209,210].

Other authors[127,203] have explored electron doping by lithium or hydrogen intercalation into $SmNiO_3$ thin films for tuning both the band gap up to 3 eV and the refractive index. Such variations are spectacular and the fact that such films can be reliably synthesized, are stable at ambient conditions and have a reversibly controlled level of doping, opens the door to the realization of a variety of photonic devices. Several device concepts have been discussed in Ref. [203]: (i) Electric-field tunable solid-state devices exploring electrochromic properties. The stability of nickelates in the presence of oxygen or moisture compares favorably to alternative organic or inorganic materials. (ii) Devices where the transparency can be reversibly controlled through electron doping to create reconfigurable photonic devices. Holograms and optical memories have been envisaged. (iii) Exploring the large range of accessible refractive indices for the control of optical absorption / transmissivity in smart windows or for radiation control allowing thermal management in space technologies. (iv) Provided that the electron-doping-induced changes are not accompanied by a structural phase transition (as suggested in Ref. [203]) this would make possible applications that take advantage of ultrafast switching such as planar optical modulators. All these device concepts raise high expectations and ask for an even better understanding to face the recurring challenge of endurance, which is inherent whenever phase transitions are involved in the technology.

Another way to develop new optical devices is the mastering of defect engineering, as described in Ref. [204] for developing active optical metasurfaces. Here, the authors use ion irradiation through a nanometer-scale mask to selectively defect engineer VO_2. This is another illustration of the potential of nano-fabrication, and it is expected that such selective ion beam engineering could also be of interest for transforming nickelates into photonic structures.

Finally, thermochromism is the property of substances to change color due to a change in temperature. This functionality can be used, for instance, to control the passing of sunlight through windows. All inorganic materials are to some extent thermochromic; however, the property is generally the most pronounced in materials that undergo an MIT. VO_2 is the most studied thermochromic compound because its MIT is the closest to room temperature. Nickelates, for which the MIT can be tuned to the vicinity around room temperature, have been proposed as promising thermochromic materials [206-208,252,253]. More research into this direction is needed to ascertain this potential.

Last but not least, more "simple" devices such as bolometers, where the power of incident electromagnetic radiation is measured via the heating of a material with a temperature-dependent electrical resistance, such as the nickelates, can also take advantage of the approaches described previously.

6.3 Magnetic properties

Due to the discovery of colossal magnetoresistance (CMR) effects in other perovskite-related systems, nickelates have also been investigated for their magnetoresistive properties [54,254]. The observed effects are rather modest when compared e.g. to manganites, with little prospect for application at this moment, even though the report of a sign reversal of magnetoresistance in a perovskite nickelate by electron doping might open new routes [234]. Over the past years, it has been proposed [235-237] that the bond/charge order in the antiferromagnetic-insulating regime of nickelates might induce improper ferroelectricity, but this theoretical prediction remains to be experimentally verified. The actual existence of an induced-ferroelectricity would turn nickelates into a type II multiferroic material [85], which are known for their high magneto-electric coupling, thus adding an interesting tunable parameter and the potential for new device concepts.

7. Wrap-up & outlook

A. Materials. Past studies of nickelates were mostly limited to polycrystalline ceramic samples synthesized under extreme conditions of oxygen pressure and high temperature, both necessary for the chemical stabilization of the perovskite phase with Ni in its nominal 3+ valence state. The absence of sizeable crystals has inhibited a closer investigation and a deeper understanding of structural details and coupling mechanism. In this regard, the synthesis of high-quality epitaxial nickelate thin films has been an essential breakthrough for further exploring the rich landscape of structural and physical properties of nickelates. High quality $LaNiO_3$ single crystals have been recently synthesized [37,38], overcoming a challenge which hampered the study of the bulk $RNiO_3$ for a long time and opening new perspectives on the investigation of the material.

Today, most literature studies focus on $LaNiO_3$, $NdNiO_3$, $SmNiO_3$ and their solid solutions. Future studies into $RNiO_3$ with smaller rare earths are desirable.

Advances in thin film synthesis techniques now pave the way toward oxide heterostructures of very high quality, increasingly comparable to that of semiconductors. Generally

speaking, heterostructures are a powerful route toward manipulation of the electronic states of transition metal oxides by exploiting strain effects, interface-driven phenomena or reduced dimensionalities. Recent works on nickelate-based superlattices have opened a variety of avenues to further control their functionalities and even realize novel collective phases. The characterization and understanding relies on state-of-the-art techniques. To date, most work has concentrated on $LaNiO_3$-based superlattices and some recent studies integrate other $RNiO_3$ compounds; in contrast, all-nickelate multilayers (not counting $LaNiO_3$) have been investigated very little. Also, the original prediction by Chaloupka and Khallilun of a superconducting phase stabilized in $RNiO_3$ films through confinement and heterostructuring[147] has yet to be confirmed. Advances in material design and fabrication techniques may allow such ideas to be further explored.

B. Advancement of understanding. In the past few years, a coherent picture of the metal-insulator transition of perovskite nickelates has emerged, and a notable agreement between experimental observations, model theories, and first-principles simulations has been reached. Today there is a deeper understanding of the key role of the O_6-breathing distortions (bond disproportionation) in the insulating state, and the nature of the exotic "charge order" that accompanies them, which does not involve any significant charge transfer between nickels but, rather, a self-doping effect resulting in oxygen holes. Admittedly, some important questions remain open, for instance, regarding the nature (and onset of) the magnetic order, the possible occurrence of multiferroic effects and the insulating behavior of ultrathin $LaNiO_3$ films. Yet, in terms of theoretical models and predictive simulation tools, it seems fair to say that today we are well equipped to tackle those remaining challenges as well as to explore the wealth of possibilities that nickelate-based nanostructures and heterostructures potentially offer.

C. Interface physics. Artificial structures, such as multilayers, either purely composed of nickelates or in combination with other functional perovskites, enrich the interface physics[12] . In such structures, emergent effects, for instance, confinement, proximity phenomena, charge transfer and particular local structures, have been observed [3,4]. We expect that an expanding theoretical and experimental understanding of exotic electronic, orbital and spin states at interfaces will extend the discussion here.

D. Applications. A large panel of potential applications for nickelate thin films has been identified. While some remain at the level of ideas or concepts, more and more reports demonstrate actual feasibility and the integration of nickelate films into devices with increasingly complex or innovative architectures. The versatility of nickelate films stems

from the fact that their properties - be they electronic, optical or opto-electronic in nature - can be modulated to a large extent by strain, chemistry, stoichiometry, electron doping, defect engineering, ionic liquid gating etc., which in turn opens a large window of functionalities. Interface physics provides the additional parameter space for improving or even extending the applications discussed for individual films and multilayers. This may also concern magnetic properties, which have, so far, been little-explored in nickelate-based devices. Several proposed devices would rely on the epitaxial integration of nickelates with Si, Ge, and other semiconductors, which is almost unexplored and certainly will need further attention in the future.

Acknowledgments

JK and JI acknowledge support from the National Research Fund, Luxembourg through a Pearl Grant (FNR/P12/4853155). This work was supported by the Swiss National Science Foundation through Division II. The research leading to these results has received funding from the European Research Council under the European Union's Seventh Framework Program (FP7/2007-2013)/ERC Grant Agreement no. 319286 (Q-MAC).

References

1 J. Mannhart and D. G. Schlom, Science **327** (5973), 1607 (2010).
2 M. Bibes, J. E. Villegas, and A. Barthélémy, Advances in Physics **60** (1), 5 (2011).
3 H. Y. Hwang, Y. Iwasa, M. Kawasaki, B. Keimer, N. Nagaosa, and Y. Tokura, Nature Materials **11** (2), 103 (2012).
4 H. Y. Hwang, MRS Bulletin **31** (1), 28 (2011).
5 M. L. Medarde, Journal of Physics-Condensed Matter **9** (8), 1679 (1997).
6 G. Catalan, Phase Transitions **81** (7-8), 729 (2008).
7 S. Middey, J. Chakhalian, P. Mahadevan, J. W. Freeland, A. J. Millis, and D. D. Sarma, in *Annual Review of Materials Research, Vol 46*, edited by D. R. Clarke (2016), Vol. 46, pp. 305.
8 R. H. Mitchell, *Perovskites Modern and Ancient*. (Almaz Press, Thunder Bay, Ontario, 2002).
9 A. M. Glazer, Acta Crystallographica, Section A (Crystal Physics, Diffraction, Theoretical and General Crystallography) **A31**, 756 (1975).
10 A. Glazer, Acta Crystallographica Section B **28** (11), 3384 (1972).
11 A. Vailionis, H. Boschker, W. Siemons, E. P. Houwman, D. H. A. Blank, G. Rijnders, and G. Koster, Physical Review B **83** (6), 064101 (2011).
12 P. Zubko, S. Gariglio, M. Gabay, P. Ghosez, and J.-M. Triscone, in *Annual Review of Condensed Matter Physics, Vol 2*, edited by J. S. Langer (2011), Vol. 2, pp. 141.
13 D. Khomskii, *Transition metal compounds*. (Cambridge University Press, 2014).
14 N. F. Mott, Proceedings of the Physical Society. Section A **62** (7), 416 (1949).
15 N. Mott, Reviews of Modern Physics **40** (4), 677 (1968).
16 J. Zaanen, G. A. Sawatzky, and J. W. Allen, Physical Review Letters **55** (4), 418 (1985).
17 A. E. Bocquet, T. Mizokawa, T. Saitoh, H. Namatame, and A. Fujimori, Physical Review B **46** (7), 3771 (1992).
18 T. Mizokawa, A. Fujimori, H. Namatame, K. Akeyama, and N. Kosugi, Physical Review B **49** (11), 7193 (1994).
19 T. Mizokawa, H. Namatame, A. Fujimori, K. Akeyama, H. Kondoh, H. Kuroda, and N. Kosugi, Physical Review Letters **67** (12), 1638 (1991).
20 J. B. Torrance, P. Lacorre, A. I. Nazzal, E. J. Ansaldo, and C. Niedermayer, Phys. Rev. B **45** (14), 8209 (1992).
21 J. A. Alonso, J. L. Garcia-Munoz, M. T. Fernandez-Diaz, M. A. G. Aranda, M. J. Martinez-Lope, and M. T. Casais, Physical Review Letters **82** (19), 3871 (1999).
22 J. A. Alonso, M. J. Martinez-Lope, M. T. Casais, J. L. Garcia-Munoz, and M. T. Fernandez-Diaz, Physical Review B **61** (3), 1756 (2000).
23 M. Medarde, M. T. Fernández-Díaz, and P. Lacorre, Physical Review B **78** (21), 212101 (2008).
24 J. L. García-Muñoz, M. A. G. Aranda, J. A. Alonso, and M. J. Martínez-Lope, Physical Review B **79** (13), 134432 (2009).

[25] H. Park, A. J. Millis, and C. A. Marianetti, Physical Review Letters **109** (15), 156402 (2012).
[26] S. Johnston, A. Mukherjee, I. Elfimov, M. Berciu, and G. A. Sawatzky, Physical Review Letters **112** (10), 106404 (2014).
[27] A. Subedi, O. E. Peil, and A. Georges, Physical Review B **91** (7) (2015).
[28] J. Varignon, M. N. Grisolia, J. Íñiguez, A. Barthélémy, and M. Bibes, npj Quantum Materials **2** (1), 21 (2017).
[29] S. Prosandeev, L. Bellaiche, and J. Iniguez, Physical Review B **85** (21) (2012).
[30] S. Yamamoto and T. Fujiwara, Journal of Physics and Chemistry of Solids **63** (6-8), 1347 (2002).
[31] A. Hampel and C. Ederer, arXiv preprint arXiv:1707.02161 (2017).
[32] R. J. Green, M. W. Haverkort, and G. A. Sawatzky, Physical Review B **94** (19), 195127 (2016).
[33] J. Perez-Cacho, J. Blasco, J. Garcia, M. Castro, and J. Stankiewicz, Journal of Physics-Condensed Matter **11** (2), 405 (1999).
[34] J. L. Garcia-Muñoz, J. Rodriguez-Carvajal, and P. Lacorre, Physical Review B **50** (2), 978 (1994).
[35] J. Rodriguez-Carvajal, S. Rosenkranz, M. Medarde, P. Lacorre, M. T. Fernandez-Diaz, F. Fauth, and V. Trounov, Physical Review B **57** (1), 456 (1998).
[36] J. L. García-Munoz, J. Rodríguez-Carvajal, P. Lacorre, and J. B. Torrance, Physical Review B **46** (8), 4414 (1992).
[37] J. Zhang, H. Zheng, Y. Ren, and J. F. Mitchell, Crystal Growth & Design **17** (5), 2730 (2017).
[38] Z. Li, H. Guo, Z. Hu, L. Zhao, C.-Y. Kuo, W. Schmidt, A. Piovano, T. Pi, D. Khomskii, and L. Tjeng, arXiv preprint arXiv:1705.02589 (2017).
[39] J. A. Alonso, M. J. Martinez-Lope, M. T. Casais, M. A. G. Aranda, and M. T. Fernandez-Diaz, Journal of the American Chemical Society **121** (20), 4754 (1999).
[40] J. B. Torrance, P. Lacorre, C. Asavaroengchai, and R. M. Metzger, Physica C: Superconductivity **182** (4-6), 351 (1991).
[41] T. Mizokawa, D. I. Khomskii, and G. A. Sawatzky, Physical Review B **61** (17), 11263 (2000).
[42] M. Medarde, A. Fontaine, J. L. García-Muñoz, J. Rodríguez-Carvajal, M. de Santis, M. Sacchi, G. Rossi, and P. Lacorre, Physical Review B **46** (23), 14975 (1992).
[43] V. Scagnoli, U. Staub, A. M. Mulders, M. Janousch, G. I. Meijer, G. Hammerl, J. M. Tonnerre, and N. Stojic, Physical Review B **73** (10), 100409 (2006).
[44] I. I. Mazin, D. I. Khomskii, R. Lengsdorf, J. A. Alonso, W. G. Marshall, R. M. Ibberson, A. Podlesnyak, M. J. Martínez-Lope, and M. M. Abd-Elmeguid, Physical Review Letters **98** (17), 176406 (2007).
[45] T. Mizokawa, A. Fujimori, T. Arima, Y. Tokura, N. Mōri, and J. Akimitsu, Physical Review B **52** (19), 13865 (1995).
[46] V. Bisogni, S. Catalano, R. J. Green, M. Gibert, R. Scherwitzl, Y. Huang, V. N. Strocov, P. Zubko, S. Balandeh, J.-M. Triscone, G. Sawatzky, and T. Schmitt, Nature Communications **7**, 13017 (2016).

[47] R. S. Dhaka, T. Das, N. C. Plumb, Z. Ristic, W. Kong, C. E. Matt, N. Xu, K. Dolui, E. Razzoli, M. Medarde, L. Patthey, M. Shi, M. Radović, and J. Mesot, Physical Review B **92** (3), 035127 (2015).
[48] P. D. C. King, H. I. Wei, Y. F. Nie, UchidaM, AdamoC, ZhuS, HeX, BozovicI, D. G. Schlom, and K. M. Shen, Nature Nanotechnology **9** (6), 443 (2014).
[49] R. Eguchi, A. Chainani, M. Taguchi, M. Matsunami, Y. Ishida, K. Horiba, Y. Senba, H. Ohashi, and S. Shin, Physical Review B **79** (11), 115122 (2009).
[50] S. Lee, R. Chen, and L. Balents, Physical Review Letters **106** (1), 016405 (2011).
[51] J. Son, B. Jalan, A. P. Kajdos, L. Balents, S. J. Allen, and S. Stemmer, Applied Physics Letters **99** (19), 192107 (2011).
[52] J. Son, P. Moetakef, J. M. LeBeau, D. Ouellette, L. Balents, S. J. Allen, and S. Stemmer, Applied Physics Letters **96** (6), 062114 (2010).
[53] R. Scherwitzl, P. Zubko, I. G. Lezama, S. Ono, A. F. Morpurgo, G. Catalan, and J.-M. Triscone, Advanced Materials **22** (48), 5517 (2010).
[54] S. D. Ha, R. Jaramillo, D. M. Silevitch, F. Schoofs, K. Kerman, J. D. Baniecki, and S. Ramanathan, Physical Review B **87** (12) (2013).
[55] S. W. Cheong, H. Y. Hwang, B. Batlogg, A. S. Cooper, and P. C. Canfield, Physica B: Condensed Matter **194** (Part 1), 1087 (1994).
[56] X. Granados, J. Fontcuberta, X. Obradors, and J. B. Torrance, Physical Review B **46** (24), 15683 (1992).
[57] X. Granados, J. Fontcuberta, X. Obradors, L. Mañosa, and J. B. Torrance, Physical Review B **48** (16), 11666 (1993).
[58] N. Gayathri, A. Raychaudhuri, X. Xu, J. Peng, and R. Greene, Journal of Physics: Condensed Matter **10** (6), 1323 (1998).
[59] M. Imada, A. Fujimori, and Y. Tokura, Reviews of Modern Physics **70** (4), 1039 (1998).
[60] S. R. Barman, A. Chainani, and D. D. Sarma, Physical Review B **49** (12), 8475 (1994).
[61] M. Medarde, P. Lacorre, K. Conder, F. Fauth, and A. Furrer, Physical Review Letters **80** (11), 2397 (1998).
[62] U. Staub, G. I. Meijer, F. Fauth, R. Allenspach, J. G. Bednorz, J. Karpinski, S. M. Kazakov, L. Paolasini, and F. d'Acapito, Physical Review Letters **88** (12), 126402 (2002).
[63] M. Medarde, C. Dallera, M. Grioni, B. Delley, F. Vernay, J. Mesot, M. Sikora, J. A. Alonso, and M. J. Martínez-Lope, Physical Review B **80** (24), 245105 (2009).
[64] J. A. Alonso, M. J. Martínez-Lope, I. A. Presniakov, A. V. Sobolev, V. S. Rusakov, A. M. Gapochka, G. Demazeau, and M. T. Fernández-Díaz, Physical Review B **87** (18), 184111 (2013).
[65] S. Prosandeev, L. Bellaiche, and J. Íñiguez, Physical Review B **85** (21), 214431 (2012).
[66] J. L. Garcia-Muñoz, J. Rodriguez-Carvajal, and P. Lacorre, Europhysics Letters **20** (3), 241 (1992).
[67] I. Vobornik, L. Perfetti, M. Zacchigna, M. Grioni, G. Margaritondo, J. Mesot, M. Medarde, and P. Lacorre, Physical Review B **60** (12), R8426 (1999).

[68] V. Scagnoli, U. Staub, Y. Bodenthin, M. García-Fernández, A. M. Mulders, G. I. Meijer, and G. Hammerl, Physical Review B **77** (11), 115138 (2008).
[69] S. Catalano, M. Gibert, V. Bisogni, O. E. Peil, F. He, R. Sutarto, M. Viret, P. Zubko, R. Scherwitzl, A. Georges, G. A. Sawatzky, T. Schmitt, and J.-M. Triscone, APL Materials **2** (11), 116110 (2014).
[70] Y. Bodenthin, U. Staub, C. Piamonteze, M. Garcia-Fernandez, M. J. Martinez-Lope, and J. A. Alonso, Journal of Physics-Condensed Matter **23** (3) (2011).
[71] A. Frano, E. Schierle, M. W. Haverkort, Y. Lu, M. Wu, S. Blanco-Canosa, U. Nwankwo, A. V. Boris, P. Wochner, G. Cristiani, H. U. Habermeier, G. Logvenov, V. Hinkov, E. Benckiser, E. Weschke, and B. Keimer, Physical Review Letters **111** (10), 106804 (2013).
[72] J. S. Zhou and J. B. Goodenough, Physical Review B **69** (15), 153105 (2004).
[73] Y. Lu, Z. Zhong, M. W. Haverkort, and P. Hansmann, Physical Review B **95** (19), 195117 (2017).
[74] J. Ruppen, J. Teyssier, I. Ardizzone, O. E. Peil, S. Catalano, M. Gibert, J. M. Triscone, A. Georges, and D. van der Marel, Physical Review B **96** (4), 045120 (2017).
[75] X. Obradors, L. M. Paulius, M. B. Maple, J. B. Torrance, A. I. Nazzal, J. Fontcuberta, and X. Granados, Physical Review B **47** (18), 12353 (1993).
[76] P. C. Canfield, J. D. Thompson, S. W. Cheong, and L. W. Rupp, Physical Review B **47** (18), 12357 (1993).
[77] J. S. Zhou, J. B. Goodenough, and B. Dabrowski, Physical Review Letters **95** (12) (2005).
[78] J. L. García-Muñoz, M. Amboage, M. Hanfland, J. A. Alonso, M. J. Martínez-Lope, and R. Mortimer, Physical Review B **69** (9), 094106 (2004).
[79] A. Y. Ramos, C. Piamonteze, H. C. N. Tolentino, N. M. Souza-Neto, O. Bunau, Y. Joly, S. Grenier, J.-P. Itié, N. E. Massa, J. A. Alonso, and M. J. Martinez-Lope, Phys. Rev. B **85** (4), 045102 (2012).
[80] Y. Ohta, T. Tohyama, and S. Maekawa, Physical Review Letters **66** (9), 1228 (1991).
[81] H. Park, A. J. Millis, and C. A. Marianetti, Physical Review B **89** (24), 245133 (2014).
[82] M. Medarde, J. Mesot, P. Lacorre, S. Rosenkranz, P. Fischer, and K. Gobrecht, Physical Review B **52** (13), 9248 (1995).
[83] J. B. Torrance, P. Lacorre, C. Asavaroengchai, and R. M. Metzger, Physica C **182** (4-6), 351 (1991).
[84] G. Giovannetti, S. Kumar, D. Khomskii, S. Picozzi, and J. van den Brink, Physical Review Letters **103** (15), 156401 (2009).
[85] D. Khomskii, Physics **2**, 20 (2009).
[86] T. Kimura, T. Goto, H. Shintani, K. Ishizaka, T. Arima, and Y. Tokura, Nature **426** (6962), 55 (2003).
[87] P. Seth, O. E. Peil, L. Pourovskii, M. Betzinger, C. Friedrich, O. Parcollet, S. Biermann, F. Aryasetiawan, and A. Georges, arXiv preprint arXiv:1707.09820 (2017).
[88] J. Ruppen, J. Teyssier, O. E. Peil, S. Catalano, M. Gibert, J. Mravlje, J. M. Triscone, A. Georges, and D. van der Marel, Physical Review B **92** (15), 155145 (2015).

89 Mercy, Bieder, J. Íñiguez, and P. Ghosez, (to be published).
90 S. L. Dudarev, G. A. Botton, S. Y. Savrasov, C. J. Humphreys, and A. P. Sutton, Physical Review B **57** (3), 1505 (1998).
91 R. Car and M. Parrinello, Physical Review Letters **55** (22), 2471 (1985).
92 E. Runge and E. K. U. Gross, Physical Review Letters **52** (12), 997 (1984).
93 S. Catalano, M. Gibert, V. Bisogni, F. He, R. Sutarto, M. Viret, P. Zubko, R. Scherwitzl, G. A. Sawatzky, T. Schmitt, and J.-M. Triscone, APL Materials **3** (6), 062506 (2015).
94 S. Yamamoto and T. Fujiwara, Journal of the Physical Society of Japan **71** (5), 1226 (2002).
95 H. Raebiger, S. Lany, and A. Zunger, Nature **453** (7196), 763 (2008).
96 G. Demazeau, A. Marbeuf, M. Pouchard, and P. Hagenmuller, Journal of Solid State Chemistry **3** (4), 582 (1971).
97 G. Catalan, R. M. Bowman, and J. M. Gregg, Physical Review B **62** (12), 7892 (2000).
98 F. Conchon, A. Boulle, R. Guinebretiere, C. Girardot, S. Pignard, J. Kreisel, F. Weiss, E. Dooryhee, and J. L. Hodeau, Applied Physics Letters **91** (19) (2007).
99 F. Conchon, A. Boulle, R. Guinebretiere, E. Dooryhee, J. L. Hodeau, C. Girardot, S. Pignard, J. Kreisel, and F. Weiss, Journal of Physics-Condensed Matter **20** (14) (2008).
100 J. A. Liu, M. Kareev, B. Gray, J. W. Kim, P. Ryan, B. Dabrowski, J. W. Freeland, and J. Chakhalian, Applied Physics Letters **96** (23) (2010).
101 J. Liu, M. Kargarian, M. Kareev, B. Gray, P. J. Ryan, A. Cruz, N. Tahir, Y.-D. Chuang, J. Guo, J. M. Rondinelli, J. W. Freeland, G. A. Fiete, and J. Chakhalian, Nature Communications **4**, 2714 (2013).
102 D. Meyers, S. Middey, M. Kareev, M. van Veenendaal, E. J. Moon, B. A. Gray, J. Liu, J. W. Freeland, and J. Chakhalian, Physical Review B **88** (7), 075116 (2013).
103 F. Y. Bruno, K. Z. Rushchanskii, S. Valencia, Y. Dumont, C. Carrétéro, E. Jacquet, R. Abrudan, S. Blügel, M. Ležaić, M. Bibes, and A. Barthélémy, Physical Review B **88** (19), 195108 (2013).
104 P.-H. Xiang, N. Zhong, C.-G. Duan, X. D. Tang, Z. G. Hu, P. X. Yang, Z. Q. Zhu, and J. H. Chu, Journal of Applied Physics **114** (24), 243713 (2013).
105 M. Hepting, M. Minola, A. Frano, G. Cristiani, G. Logvenov, E. Schierle, M. Wu, M. Bluschke, E. Weschke, H. U. Habermeier, E. Benckiser, M. Le Tacon, and B. Keimer, Physical Review Letters **113** (22) (2014).
106 M. K. Stewart, J. Liu, M. Kareev, J. Chakhalian, and D. N. Basov, Physical Review Letters **107** (17), 176401 (2011).
107 F. Conchon, A. Boulle, R. Guinebretiere, E. Dooryhee, J. L. Hodeau, C. Girardot, S. Pignard, J. Kreisel, F. Weiss, L. Libralesso, and T. L. Lee, Journal of Applied Physics **103** (12) (2008).
108 J. Y. Zhang, H. Kim, E. Mikheev, A. J. Hauser, and S. Stemmer, **6**, 23652 (2016).
109 E. Mikheev, A. J. Hauser, B. Himmetoglu, N. E. Moreno, A. Janotti, C. G. Van de Walle, and S. Stemmer, Science Advances **1** (10) (2015).
110 S. Okamoto, Physical Review Letters **110** (6), 066403 (2013).
111 S. Okamoto, W. Zhu, Y. Nomura, R. Arita, D. Xiao, and N. Nagaosa, Physical Review B **89** (19), 195121 (2014).

[112] J. L. Blok, X. Wan, G. Koster, D. H. A. Blank, and G. Rijnders, Applied Physics Letters **99** (15), 151917 (2011).

[113] S. Middey, P. Rivero, D. Meyers, M. Kareev, X. Liu, Y. Cao, J. W. Freeland, S. Barraza-Lopez, and J. Chakhalian, Scientific Reports **4**, 6819 (2014).

[114] S. Middey, D. Meyers, M. Kareev, E. J. Moon, B. A. Gray, X. Liu, J. W. Freeland, and J. Chakhalian, Applied Physics Letters **101** (26), 261602 (2012).

[115] M. Gibert, P. Zubko, R. Scherwitzl, J. Íñiguez, and J.-M. Triscone, Nature Materials **11** (3), 195 (2012).

[116] T. H. Kim, D. Puggioni, Y. Yuan, L. Xie, H. Zhou, N. Campbell, P. J. Ryan, Y. Choi, J. W. Kim, J. R. Patzner, S. Ryu, J. P. Podkaminer, J. Irwin, Y. Ma, C. J. Fennie, M. S. Rzchowski, X. Q. Pan, V. Gopalan, J. M. Rondinelli, and C. B. Eom, Nature **533** (7601), 68 (2016).

[117] S. Middey, D. Meyers, D. Doennig, M. Kareev, X. Liu, Y. Cao, Z. Yang, J. Shi, L. Gu, P. J. Ryan, R. Pentcheva, J. W. Freeland, and J. Chakhalian, Physical Review Letters **116** (5), 056801 (2016).

[118] M. Gibert, M. Viret, P. Zubko, N. Jaouen, J. M. Tonnerre, A. Torres-Pardo, S. Catalano, A. Gloter, O. Stephan, and J. M. Triscone, Nature Communications **7**, 11227 (2016).

[119] X. K. Lian, F. Chen, X. L. Tan, P. F. Chen, L. F. Wang, G. Y. Gao, S. W. Jin, and W. B. Wu, Applied Physics Letters **103**, 172110 (2013).

[120] F. He, B. O. Wells, Z. G. Ban, S. P. Alpay, S. Grenier, S. M. Shapiro, W. Si, A. Clark, and X. X. Xi, Physical Review B **70** (23), 235405 (2004).

[121] A. Rüegg and G. A. Fiete, Physical Review B **84** (20), 201103 (2011).

[122] K.-Y. Yang, W. Zhu, D. Xiao, S. Okamoto, Z. Wang, and Y. Ran, Physical Review B **84** (20), 201104 (2011).

[123] D. Doennig, W. E. Pickett, and R. Pentcheva, Phys. Rev. B **89** (12), 121110 (2014).

[124] J. L. García-Muñoz, M. Suaaidi, M. J. Martínez-Lope, and J. A. Alonso, Physical Review B **52** (18), 13563 (1995).

[125] I. V. Nikulin, M. A. Novojilov, A. R. Kaul, S. N. Mudretsova, and S. V. Kondrashov, *Oxygen nonstoichiometry of NdNiO3−δ and SmNiO3−δ*. (2004), pp.775.

[126] J. Shi, S. D. Ha, Y. Zhou, F. Schoofs, and S. Ramanathan, Nature Communications **4** (2013).

[127] J. Shi, Y. Zhou, and S. Ramanathan, Nature Communications **5**, 4860 (2014).

[128] Y. Zhou, X. Guan, H. Zhou, K. Ramadoss, S. Adam, H. Liu, S. Lee, J. Shi, M. Tsuchiya, D. D. Fong, and S. Ramanathan, Nature **534** (7606), 231 (2016).

[129] S. Heo, C. Oh, J. Son, and H. M. Jang, Scientific Reports **7** (1), 4681 (2017).

[130] R. Scherwitzl, P. Zubko, C. Lichtensteiger, and J. M. Triscone, Applied Physics Letters **95** (22), 222114 (2009).

[131] J. Son, S. Rajan, S. Stemmer, and S. J. Allen, Journal of Applied Physics **110** (8) (2011).

[132] S. H. Lee, M. Kim, S. D. Ha, J.-W. Lee, S. Ramanathan, and S. Tiwari, Applied Physics Letters **102** (7), 072102 (2013).

[133] M. S. J. Marshall, A. Malashevich, A. S. Disa, M.-G. Han, H. Chen, Y. Zhu, S. Ismail-Beigi, F. J. Walker, and C. H. Ahn, Physical Review Applied **2** (5), 051001 (2014).

134 X. Chen, X. Zhang, M. A. Koten, H. Chen, Z. Xiao, L. Zhang, J. E. Shield, P. A. Dowben, and X. Hong, Advanced Materials **29** (31), 1701385 (2017).
135 L. Zhang, X. G. Chen, H. J. Gardner, M. A. Koten, J. E. Shield, and X. Hong, Applied Physics Letters **107** (15), 152906 (2015).
136 A. D. Caviglia, R. Scherwitzl, P. Popovich, W. Hu, H. Bromberger, R. Singla, M. Mitrano, M. C. Hoffmann, S. Kaiser, P. Zubko, S. Gariglio, J. M. Triscone, M. Först, and A. Cavalleri, Phys. Rev. Lett. **108** (13), 136801 (2012).
137 W. Hu, S. Catalano, M. Gibert, J. M. Triscone, and A. Cavalleri, Physical Review B **93** (16), 161107 (2016).
138 A. D. Caviglia, M. Först, R. Scherwitzl, V. Khanna, H. Bromberger, R. Mankowsky, R. Singla, Y. D. Chuang, W. S. Lee, O. Krupin, W. F. Schlotter, J. J. Turner, G. L. Dakovski, M. P. Minitti, J. Robinson, V. Scagnoli, S. B. Wilkins, S. A. Cavill, M. Gibert, S. Gariglio, P. Zubko, J. M. Triscone, J. P. Hill, S. S. Dhesi, and A. Cavalleri, Physical Review B **88** (22), 220401 (2013).
139 M. Forst, A. D. Caviglia, R. Scherwitzl, R. Mankowsky, P. Zubko, V. Khanna, H. Bromberger, S. B. Wilkins, Y. D. Chuang, W. S. Lee, W. F. Schlotter, J. J. Turner, G. L. Dakovski, M. P. Minitti, J. Robinson, S. R. Clark, D. Jaksch, J. M. Triscone, J. P. Hill, S. S. Dhesi, and A. Cavalleri, Nature Materials **14**, 883 (2015).
140 M. Först, K. R. Beyerlein, R. Mankowsky, W. Hu, G. Mattoni, S. Catalano, M. Gibert, O. Yefanov, J. N. Clark, A. Frano, J. M. Glownia, M. Chollet, H. Lemke, B. Moser, S. P. Collins, S. S. Dhesi, A. D. Caviglia, J. M. Triscone, and A. Cavalleri, Physical Review Letters **118** (2), 027401 (2017).
141 R. Scherwitzl, S. Gariglio, M. Gabay, P. Zubko, M. Gibert, and J. M. Triscone, Physical Review Letters **106** (24), 246403 (2011).
142 H. K. Yoo, S. I. Hyun, Y. J. Chang, L. Moreschini, C. H. Sohn, H.-D. Kim, A. Bostwick, E. Rotenberg, J. H. Shim, and T. W. Noh, Physical Review B **93** (3), 035141 (2016).
143 J. Fowlie, M. Gibert, G. Tieri, A. Gloter, J. Íñiguez, A. Filippetti, S. Catalano, S. Gariglio, A. Schober, M. Guennou, J. Kreisel, O. Stéphan, and J.-M. Triscone, Advanced Materials **29** (18), 1605197 (2017).
144 D. P. Kumah, A. S. Disa, J. H. Ngai, H. Chen, A. Malashevich, J. W. Reiner, S. Ismail-Beigi, F.-J. Walker, and C. H. Ahn, Advanced Materials **26** (12), 1935 (2014).
145 M. C. Weber, M. Guennou, N. Dix, D. Pesquera, F. Sánchez, G. Herranz, J. Fontcuberta, L. López-Conesa, S. Estradé, F. Peiró, J. Iñiguez, and J. Kreisel, Physical Review B **94** (1), 014118 (2016).
146 J. Chakhalian, J. M. Rondinelli, J. Liu, B. A. Gray, M. Kareev, E. J. Moon, N. Prasai, J. L. Cohn, M. Varela, I. C. Tung, M. J. Bedzyk, S. G. Altendorf, F. Strigari, B. Dabrowski, L. H. Tjeng, P. J. Ryan, and J. W. Freeland, Physical Review Letters **107** (11), 116805 (2011).
147 J. Chaloupka and G. Khaliullin, Physical Review Letters **100** (1), 016404 (2008).
148 S. J. May, J. W. Kim, J. M. Rondinelli, E. Karapetrova, N. A. Spaldin, A. Bhattacharya, and P. J. Ryan, Physical Review B **82** (1), 014110 (2010).
149 O. E. Peil, M. Ferrero, and A. Georges, Physical Review B **90** (4), 045128 (2014).

150 P. Hansmann, A. Toschi, X. Yang, O. K. Andersen, and K. Held, Physical Review B **82** (23), 235123 (2010).
151 P. Hansmann, X. Yang, A. Toschi, G. Khaliullin, O. K. Andersen, and K. Held, Physical Review Letters **103** (1), 016401 (2009).
152 M. Wu, E. Benckiser, M. W. Haverkort, A. Frano, Y. Lu, U. Nwankwo, S. Brück, P. Audehm, E. Goering, S. Macke, V. Hinkov, P. Wochner, G. Christiani, S. Heinze, G. Logvenov, H. U. Habermeier, and B. Keimer, Physical Review B **88** (12), 125124 (2013).
153 E. Benckiser, M. W. Haverkort, S. Brück, E. Goering, S. Macke, A. Frañó, X. Yang, O. K. Andersen, G. Cristiani, H.-U. Habermeier, A. V. Boris, I. Zegkinoglou, P. Wochner, H.-J. Kim, V. Hinkov, and B. Keimer, Nature Materials **10** (3), 189 (2011).
154 J. W. Freeland, J. Liu, M. Kareev, B. Gray, J. W. Kim, P. Ryan, R. Pentcheva, and J. Chakhalian, Europhysics Letters **96**, 57004 (2011).
155 H. Chen, D. P. Kumah, A. S. Disa, F. J. Walker, C. H. Ahn, and S. Ismail-Beigi, Physical Review Letters **110** (18), 186402 (2013).
156 A. S. Disa, D. P. Kumah, A. Malashevich, H. Chen, D. A. Arena, E. D. Specht, S. Ismail-Beigi, F. J. Walker, and C. H. Ahn, Physical Review Letters **114** (2), 026801 (2015).
157 M. J. Han, X. Wang, C. A. Marianetti, and A. J. Millis, Physical Review Letters **107** (20), 206804 (2011).
158 F. Y. Bruno, M. Gibert, S. M. Walker, O. E. Peil, A. d. l. Torre, S. Riccò, Z. Wang, S. Catalano, A. Tamai, F. Bisti, V. N. Strocov, J.-M. Triscone, and F. Baumberger, APL Materials **5** (1), 016101 (2017).
159 S. J. May, T. S. Santos, and A. Bhattacharya, Physical Review B **79** (11), 115127 (2009).
160 J. Hwang, J. Y. Zhang, J. Son, and S. Stemmer, Applied Physics Letters **100** (19) (2012).
161 A. V. Boris, Y. Matiks, E. Benckiser, A. Frano, P. Popovich, V. Hinkov, P. Wochner, M. Castro-Colin, E. Detemple, V. K. Malik, C. Bernhard, T. Prokscha, A. Suter, Z. Salman, E. Morenzoni, G. Cristiani, H.-U. Habermeier, and B. Keimer, Science **332** (6032), 937 (2011).
162 Y. Lu, A. Frano, M. Bluschke, M. Hepting, S. Macke, J. Strempfer, P. Wochner, G. Cristiani, G. Logvenov, H. U. Habermeier, M. W. Haverkort, B. Keimer, and E. Benckiser, Physical Review B **93** (16), 165121 (2016).
163 H. Tanaka, N. Okawa, and T. Kawai, Solid State Communications **110** (4), 191 (1999).
164 K. R. Nikolaev, A. Y. Dobin, I. N. Krivorotov, W. K. Cooley, A. Bhattacharya, A. L. Kobrinskii, L. I. Glazman, R. M. Wentzovitch, E. D. Dahlberg, and A. M. Goldman, Physical Review Letters **85** (17), 3728 (2000).
165 J. Hoffman, I. C. Tung, B. B. Nelson-Cheeseman, M. Liu, J. W. Freeland, and A. Bhattacharya, Physical Review B **88** (14), 144411 (2013).
166 A. J. Grutter, H. Yang, B. J. Kirby, M. R. Fitzsimmons, J. A. Aguiar, N. D. Browning, C. A. Jenkins, E. Arenholz, V. V. Mehta, U. S. Alaan, and Y. Suzuki, Physical Review Letters **111** (8), 087202 (2013).

[167] C. Piamonteze, M. Gibert, J. Heidler, J. Dreiser, S. Rusponi, H. Brune, J. M. Triscone, F. Nolting, and U. Staub, Physical Review B **92** (1), 014426 (2015).

[168] J. C. Rojas Sánchez, B. Nelson-Cheeseman, M. Granada, E. Arenholz, and L. B. Steren, Physical Review B **85** (9), 094427 (2012).

[169] M. Gibert, M. Viret, A. Torres-Pardo, C. Piamonteze, P. Zubko, N. Jaouen, J. M. Tonnerre, A. Mougin, J. Fowlie, S. Catalano, A. Gloter, O. Stéphan, and J. M. Triscone, Nano Letters **15** (11), 7355 (2015).

[170] S. Dong and E. Dagotto, Physical Review B **87** (19), 195116 (2013).

[171] A. T. Lee and M. J. Han, Physical Review B **88** (3), 035126 (2013).

[172] K. R. Nikolaev, A. Bhattacharya, P. A. Kraus, V. A. Vas'ko, W. K. Cooley, and A. M. Goldman, Applied Physics Letters **75** (1), 118 (1999).

[173] J. D. Hoffman, B. J. Kirby, J. Kwon, G. Fabbris, D. Meyers, J. W. Freeland, I. Martin, O. G. Heinonen, P. Steadman, H. Zhou, C. M. Schlepütz, M. P. M. Dean, S. G. E. te Velthuis, J.-M. Zuo, and A. Bhattacharya, Physical Review X **6** (4), 041038 (2016).

[174] M. N. Grisolia, J. Varignon, G. Sanchez-Santolino, A. Arora, S. Valencia, M. Varela, R. Abrudan, E. Weschke, E. Schierle, J. E. Rault, J. P. Rueff, A. Barthelemy, J. Santamaria, and M. Bibes, Nat Phys **12** (5), 484 (2016).

[175] H. Chen, A. J. Millis, and C. A. Marianetti, Physical Review Letters **111** (11), 116403 (2013).

[176] Y. W. Cao, X. R. Liu, M. Kareev, D. Choudhury, S. Middey, D. Meyers, J. W. Kim, P. J. Ryan, J. W. Freeland, and J. Chakhalian, Nature Communications **7** (2016).

[177] C. Girardot, S. Pignard, F. Weiss, and J. Kreisel, Appl. Phys. Lett. **98**, 241903 (2011).

[178] E. Dagotto, Science **309** (5732), 257 (2005).

[179] M. Nakano, K. Shibuya, D. Okuyama, T. Hatano, S. Ono, M. Kawasaki, Y. Iwasa, and Y. Tokura, Nature **487** (7408), 459 (2012).

[180] J. Jeong, N. Aetukuri, T. Graf, T. D. Schladt, M. G. Samant, and S. S. P. Parkin, Science **339** (6126), 1402 (2013).

[181] N. Shukla, A. V. Thathachary, A. Agrawal, H. Paik, A. Aziz, D. G. Schlom, S. K. Gupta, R. Engel-Herbert, and S. Datta, Nature Communications **6** (2015).

[182] Z. Yang, C. Y. Ko, and S. Ramanathan, in *Annual Review of Materials Research, Vol 41*, edited by D. R. Clarke and P. Fratzl (2011), Vol. 41, pp. 337.

[183] R. N. Singh, L. Bahadur, J. P. Pandey, S. P. Singh, P. Chartier, and G. Poillerat, Journal of Applied Electrochemistry **24** (2), 149 (1994).

[184] Y. Cao, B. P. Lin, Y. Sun, H. Yang, and X. Q. Zhang, Electrochimica Acta **174**, 41 (2015).

[185] L. Hu, Y. F. Deng, K. Liang, X. J. Liu, and W. C. Hu, Journal of Solid State Electrochemistry **19** (3), 629 (2015).

[186] D. K. Hwang, S. Kim, J. H. Lee, I. S. Hwang, and I. D. Kim, Journal of Materials Chemistry **21** (6), 1959 (2011).

[187] K. Liang, N. Wang, M. Zhou, Z. Y. Cao, T. L. Gu, Q. Zhang, X. Z. Tang, W. C. Hu, and B. Q. Wei, Journal of Materials Chemistry A **1** (34), 9730 (2013).

[188] X. Liu, G. Du, J. L. Zhu, Z. F. Zeng, and X. H. Zhu, Applied Surface Science **384**, 92 (2016).

189 F. Y. Bruno, S. Boyn, S. Fusil, S. Girod, C. Carretero, M. Marinova, A. Gloter, S. Xavier, C. Deranlot, M. Bibes, A. Barthelemy, and V. Garcia, Advanced Electronic Materials **2** (3) (2016).
190 B. V. Mistry, R. Pinto, and U. S. Joshi, Journal of Materials Science-Materials in Electronics **27** (2), 1812 (2016).
191 H. N. Xu, Y. Liu, B. Xu, Y. D. Xia, G. S. Wang, J. Yin, and Z. G. Liu, Journal of Physics D-Applied Physics **49** (37) (2016).
192 Z. W. Dong, S. P. Pai, R. Ramesh, T. Venkatesan, M. Johnson, Z. Y. Chen, A. Cavanaugh, Y. G. Zhao, X. L. Jiang, R. P. Sharma, S. Ogale, and R. L. Greene, Journal of Applied Physics **83** (11), 6780 (1998).
193 D. H. Bao, N. Wakiya, K. Shinozaki, N. Mizutani, and X. Yao, Journal of Applied Physics **90** (1), 506 (2001).
194 S. T. Zhang, X. J. Zhang, H. W. Cheng, Y. F. Chen, Z. G. Liu, N. B. Ming, X. B. Hu, and J. Y. Wang, Applied Physics Letters **83** (21), 4378 (2003).
195 J. Ge, X. L. Dong, Y. Chen, F. Cao, and G. S. Wang, Applied Physics Letters **102** (14) (2013).
196 H. Han, J. Zhong, S. Kotru, P. Padmini, X. Y. Song, and R. K. Pandey, Applied Physics Letters **88** (9) (2006).
197 A. D. Li, C. Z. Ge, P. Lu, D. Wu, S. B. Xiong, and N. B. Ming, Applied Physics Letters **70** (12), 1616 (1997).
198 K. V. R. Prasad, K. B. R. Varma, A. R. Raju, K. M. Satyalakshmi, R. M. Mallya, and M. S. Hegde, Applied Physics Letters **63** (14), 1898 (1993).
199 K. Kim, M. Paranthaman, D. P. Norton, T. Aytug, C. Cantoni, A. A. Gapud, A. Goyal, and D. K. Christen, Superconductor Science & Technology **19** (4), R23 (2006).
200 G. Z. Sun, P. H. Wu, Y. Feng, Z. M. Ji, S. Z. Yang, M. Wang, W. W. Xu, and L. Kang, Thin Solid Films **471** (1-2), 248 (2005).
201 T. Aytug, J. Z. Wu, C. Cantoni, D. T. Verebelyi, E. D. Specht, M. Paranthaman, D. P. Norton, D. K. Christen, R. E. Ericson, and C. L. Thomas, Applied Physics Letters **76** (6), 760 (2000).
202 Q. He, D. K. Christen, R. Feenstra, D. P. Norton, M. Paranthaman, E. D. Specht, D. F. Lee, A. Goyal, and D. M. Kroeger, Physica C **314** (1-2), 105 (1999).
203 Z. Y. Li, Y. Zhou, H. Qi, Q. W. Pan, Z. Zhang, N. N. Shi, M. Lu, A. Stein, C. Y. Li, S. Ramanathan, and N. F. Yu, Advanced Materials **28** (41), 9117 (2016).
204 J. Rensberg, S. Zhang, Y. Zhou, A. S. McLeod, C. Schwarz, M. Goldflam, M. K. Liu, J. Kerbusch, R. Nawrodt, S. Ramanathan, D. N. Basov, F. Capasso, C. Ronning, and M. A. Kats, Nano Letters **16** (2), 1050 (2016).
205 L. Wang, L. Chang, X. Yin, L. You, J.-L. Zhao, H. Guo, K. Jin, K. Ibrahim, J. Wang, A. Rusydi, and J. Wang, Applied Physics Letters **110** (4), 043504 (2017).
206 B. D. Ngom, J. B. K. Kana, O. Nemraoui, N. Manyala, M. Maaza, R. Mdjoe, and A. C. Beye, in *Laser and Plasma Applications in Materials Science*, edited by E. H. Amara, S. Boudjemai, and D. Doumaz (2008), Vol. 1047, pp. 280.
207 T. Shao, Z. M. Qi, Y. Y. Wang, Y. Y. Li, M. Yang, Y. Wang, G. B. Zhang, and M. Liu, Applied Physics Letters **107** (2) (2015).
208 P. Kiria, G. Hyett, and R. Binions, Advanced Materials Letters **1** (2), 86 (2010).

[209] L. Chang, L. Wang, L. You, Y. Zhou, L. Fang, S. W. Wang, and J. L. Wang, Journal of Physics D-Applied Physics **49** (44) (2016).
[210] L. Wang, S. Dash, L. Chang, L. You, Y. Q. Peng, X. He, K. J. Jin, Y. Zhou, H. G. Ong, P. Ren, S. W. Wang, L. Chen, and J. L. Wang, Acs Applied Materials & Interfaces **8** (15), 9769 (2016).
[211] Y. Zhou, X. F. Guan, H. Zhou, K. Ramadoss, S. Adam, H. J. Liu, S. Lee, J. Shi, M. Tsuchiya, D. D. Fong, and S. Ramanathan, Nature **534** (7606), 231 (2016).
[212] J. B. Goodenough, Reports on Progress in Physics **67** (11), 1915 (2004).
[213] H. Y. Ma, B. G. Wang, Y. S. Fan, and W. C. Hong, Energies **7** (10), 6549 (2014).
[214] J. Zhang, Y. B. Zhao, X. Zhao, Z. L. Liu, and W. Chen, Scientific Reports **4**, 6 (2014).
[215] J. Ma, Y. Liu, Y. Liu, Y. Yan, and P. Zhang, Fuel Cells **8** (6), 394 (2008).
[216] R. N. Singh, A. N. Jain, S. K. Tiwari, G. Poillerat, and P. Chartier, Journal of Applied Electrochemistry **25** (12), 1133 (1995).
[217] S. D. Ha, G. H. Aydogdu, and S. Ramanathan, Applied Physics Letters **98** (1) (2011).
[218] C. Oh, S. Heo, H. M. Jang, and J. Son, Applied Physics Letters **108** (12) (2016).
[219] P. Pandey, R. Rana, S. Tripathi, and D. S. Rana, Applied Physics Letters **103** (3) (2013).
[220] S. D. Ha, J. Shi, Y. Meroz, L. Mahadevan, and S. Ramanathan, Physical Review Applied **2** (6) (2014).
[221] S. H. Lee, M. Kim, S. D. Ha, J.-W. Lee, S. Ramanathan, and S. Tiwari, Applied Physics Letters **102** (7), 072102 (2013).
[222] S. Asanuma, P. H. Xiang, H. Yamada, H. Sato, I. H. Inoue, H. Akoh, A. Sawa, K. Ueno, H. Shimotani, H. Yuan, M. Kawasaki, and Y. Iwasa, Applied Physics Letters **97** (14) (2010).
[223] T. R. Ling, Z. B. Chen, and M. D. Lee, Catalysis Today **26** (1), 79 (1995).
[224] X. C. Lu, T. X. Xu, and X. H. Dong, Sensors and Actuators B-Chemical **67** (1-2), 24 (2000).
[225] R. Bouregba, G. Le Rhun, and G. Poullain, Integrated Ferroelectrics **70**, 67 (2005).
[226] F. Hou, Y. N. Qin, and T. X. Xu, Rare Metal Materials and Engineering **31**, 296 (2002).
[227] F. Hou, Y. N. Qin, T. X. Xu, and M. X. Xu, Journal of Electroceramics **8** (3), 243 (2002).
[228] T. Kobayashi, R. Kondou, K. Nakamura, M. Ichiki, and R. Maeda, Japanese Journal of Applied Physics Part 1-Regular Papers Brief Communications & Review Papers **46** (10B), 7073 (2007).
[229] A. Lazauskas, J. Baltrusaitis, V. Grigaliunas, and I. Prosycevas, Applied Surface Science **344**, 159 (2015).
[230] H. L. Lung, S. C. Lai, H. Y. Lee, T. B. Wu, R. Liu, and C. Y. Lu, Ieee Transactions on Electron Devices **51** (6), 920 (2004).
[231] C. Suo, C. J. Gao, X. Y. Wu, Y. Zuo, X. C. Wang, and J. F. Jia, Rsc Advances **5** (112), 92107 (2015).
[232] M. Sygnatowicz, M. Snure, and A. Tiwari, Journal of Crystal Growth **310** (15), 3590 (2008).

[233] B. J. Wang, S. Q. Gu, Y. P. Ding, Y. L. Chu, Z. Zhang, X. Ba, Q. L. Zhang, and X. R. Li, Analyst **138** (1), 362 (2013).
[234] K. Ramadoss, N. Mandal, X. Dai, Z. Wan, Y. Zhou, L. Rokhinson, Y. P. Chen, J. P. Hu, and S. Ramanathan, Physical Review B **94** (23), 6 (2016).
[235] S. W. Cheong and M. Mostovoy, Nature Materials **6**, 13 (2007).
[236] J. V. d. Brink and D. I. Khomskii, Journal of Physics: Condensed Matter **20** (43), 249 (2008).
[237] G. Catalan, Phase Transitions **81**, 729 (2008).
[238] S. D. Ha, J. Shi, Y. Meroz, L. Mahadevan, and S. Ramanathan, Physical Review Applied **2** (6), 064003 (2014).
[239] C. Guerrero, F. Sánchez, C. Ferrater, J. Roldán, M. V. García-Cuenca, and M. Varela, Applied Surface Science **168** (1), 219 (2000).
[240] R. Scherwitzl, S. Gariglio, M. Gabay, P. Zubko, M. Gibert, and J. M. Triscone, Physical Review Letters **106** (24) (2011).
[241] J. Fowlie, M. Gibert, G. Tieri, A. Gloter, J. Íñiguez, A. Filippetti, S. Catalano, S. Gariglio, A. Schober, M. Guennou, J. Kreisel, O. Stéphan, and J.-M. Triscone, Advanced Materials, DOI: 10.1002/adma.201605197 (2017).
[242] S. H. Jo, T. Chang, I. Ebong, B. B. Bhadviya, P. Mazumder, and W. Lu, Nano Letters **10** (4), 1297 (2010).
[243] A. Sawa, Materials Today **11** (6), 28 (2008).
[244] C. L. O., IEEE Trans. Circuit Theory **18**, 507 (1971).
[245] T. Driscoll, H.-T. Kim, B.-G. Chae, M. D. Ventra, and D. N. Basov, Applied Physics Letters **95** (4), 043503 (2009).
[246] D. B. Strukov, G. S. Snider, D. R. Stewart, and R. S. Williams, Nature **453** (7191), 80 (2008).
[247] A. Chanthbouala, V. Garcia, R. O. Cherifi, K. Bouzehouane, S. Fusil, X. Moya, S. Xavier, H. Yamada, C. Deranlot, N. D. Mathur, M. Bibes, A. Barthélémy, and J. Grollier, Nat Mater **11** (10), 860 (2012).
[248] D. J. Kim, H. Lu, S. Ryu, C. W. Bark, C. B. Eom, E. Y. Tsymbal, and A. Gruverman, Nano Letters **12** (11), 5697 (2012).
[249] F. Messerschmitt, M. Kubicek, S. Schweiger, and J. L. M. Rupp, Advanced Functional Materials **24** (47), 7448 (2014).
[250] S. Schweiger, M. Kubicek, F. Messerschmitt, C. Murer, and J. L. M. Rupp, Acs Nano **8** (5), 5032 (2014).
[251] M. D. Ventra, Y. V. Pershin, and L. O. Chua, Proceedings of the IEEE **97** (10), 1717 (2009).
[252] A. Boileau, F. Capon, P. Laffez, S. Barrat, J. L. Endrino, R. E. Galindo, D. Horwat, and J. F. Pierson, The Journal of Physical Chemistry C **118** (11), 5908 (2014).
[253] C. Napierala - Dutfoy, M. Edely, P. Laffez, and L. Sauques, *Thermo-optical effect of Nd0.3Sm0.7NiO3 ceramic in the infrared range*. (2009), pp.1498.
[254] K. Ramadoss, N. Mandal, X. Dai, Z. Wan, Y. Zhou, L. Rokhinson, Y. P. Chen, J. P. Hu, and S. Ramanathan, Physical Review B **94** (23) (2016).